Check for updates

Received: 8 October 2024 | Revised: 15 April 2025 | Accepted: 20 April 2025

DOI: 10.1002/qj.5011

Quarterly Journal of the Royal Meteorological Society RMetS

RESEARCH ARTICLE

Rapid versus slow intensification of idealized tropical cyclones using soundings from reanalysis

Samantha Nebylitsa | **David S. Nolan** | **Brian D. McNoldy** | **Sharanya J. Majumdar**

Rosenstiel School of Marine, Atmospheric, and Earth Science, University of Miami, Miami, Florida, USA

Correspondence
Samantha Nebylitsa, Rosenstiel School of Marine, Atmospheric, and Earth Science, University of Miami, Miami, FL, USA.
Email: sxn573@miami.edu

Funding information
Office of Naval Research, Grant/Award Number: N00014-20-1-2075

Abstract

Low vertical wind shear and high mid-tropospheric humidity are accepted to usually be conducive for the rapid intensification of tropical cyclones (TCs). Climatologically averaged environmental wind and moisture profiles around intensifying TCs are used to be more representative of TC environments than previous idealized studies. The structural and thermodynamic differences between ensembles of rapidly (RI) and slowly (SI) intensifying storms are analyzed. On average, RI storms have lower vertical tilt, are more symmetric, and less ventilated at onset than SI storms. SI is characterized by abundant downdraft ventilation left of shear and inner-core radial ventilation upshear right. RI events contain more points with greater reflectivities and updrafts compared to SI events, which have more points with lower reflectivity values and downdrafts. Despite these significant differences at onset, the RI and SI ensembles are nearly identical just 24 hours prior. Most notably, the rapid vertical alignment and symmeterization of precipitation in the 12 hours prior to onset was found to be a better indicator of RI versus SI. This result suggests that it is the evolution of these variables that provides a signal to the expected intensification rate, and not simply a standalone value or pattern.

KEYWORDS

asymmetry, idealized model, shear, tilt, tropical cyclone, ventilation

1 | INTRODUCTION

The environment around tropical cyclones (TCs) significantly influences the intensification rate of the storm. For rapid intensification (RI) events, defined as an increase in the 10-m, 1-min maximum sustained winds of at least 30 kt in 24 hours (Kaplan & DeMaria, 2003), the consensus is that RI is more likely in environments of weaker vertical wind shear (hereafter referred to as "shear"), moister mid-levels, and higher sea surface temperatures (SSTs) (e.g., Hendricks *et al.*, 2010; Kaplan *et al.*, 2010; Kaplan & DeMaria, 2003; Majumdar *et al.*, 2023; Nebylitsa *et al.*, 2023; Rios-Berrios & Torn, 2017). Strong shear can inhibit TC intensification (DeMaria & Kaplan, 1994; Hendricks *et al.*, 2010) as it tilts the TC in the vertical, leading to an asymmetric secondary circulation

This is an open access article under the terms of the Creative Commons Attribution-NonCommercial-NoDerivs License, which permits use and distribution in any medium, provided the original work is properly cited, the use is non-commercial and no modifications or adaptations are made.
© 2025 The Author(s). *Quarterly Journal of the Royal Meteorological Society* published by John Wiley & Sons Ltd on behalf of Royal Meteorological Society.

(Rios-Berrios & Torn, 2017) which may hinder the feedback between surface fluxes and latent heat release that TC intensification theories are based upon (Emanuel, 1986; Molinari *et al.*, 2004). TCs also need adequate environmental moisture to intensify, as low-entropy air can inhibit the TC heat engine (Tang & Emanuel, 2010). Despite this agreement in observational, reanalysis, and modeling studies, there are still many nuances around the specific conditions in which RI occurs, including smaller-scale internal factors that pose a modeling and predictability challenge.

The relationship between TCs and shear is complex (Rios-Berrios *et al.*, 2024 and references therein). Modeling studies have shown that higher values of shear inhibit RI and increase the uncertainty in the timing and rate of intensification (Tao & Zhang, 2015; Zhang & Tao, 2013), but upper-level winds and shear direction can also influence intensification rates (DeMaria, 2010; Finocchio *et al.*, 2016). Lower-level shear induces low-level vortex tilt, which allows low-equivalent potential temperature (θ_e) air to penetrate further within the radius of maximum winds (RMW) and inhibits further intensification (Finocchio *et al.*, 2016; Finocchio & Majumdar, 2017; Vigh & Schubert, 2009). Larger tilt can also erode the warm core at upper levels resulting in a decrease in intensity (DeMaria, 1996; Frank & Ritchie, 2001; Kwon & Frank, 2008).

Alvey III *et al.* (2020) found that the vortex tilt of intensifying ensemble members of modeled hurricane *Edouard* (2014) was notably lower than for non-intensifying members, despite having comparable shear values. The larger spread in environmental humidity also played a role in which ensemble members intensified (also shown by Munsell *et al.*, 2013; Rios-Berrios *et al.*, 2016a, 2016b). Successful RI ensemble members had more deep convection downshear which favors vortex alignment and allows convection to move into the upshear quadrants due to increased moisture from evaporation (Alvey III *et al.*, 2020; Rappin & Nolan, 2012; Richardson *et al.*, 2022). While many idealized studies have found that tilt reduction and vortex alignment are precursors to RI (e.g., Rappin & Nolan, 2012; Rios-Berrios *et al.*, 2018; Schecter, 2022; Zhang & Tao, 2013) there is still no consensus on whether vortex alignment is a cause or effect of intensity change (Judt *et al.*, 2023). Additionally, observations from airborne Doppler radar indicate no statistical difference in observed tilt magnitude for intensifying versus steady-state storms (Rogers *et al.*, 2013). Fischer *et al.* (2024) discovered a weak relationship between vortex tilt and intensity change, although the relationship trend was more robust when weak TCs were considered.

Vortex tilting increases low-level convergence downshear and leads to a displacement of the convection (Finocchio *et al.*, 2016; Jones, 1995). Convection is suppressed on the upshear side of the storm with updrafts occurring on the downshear side creating an asymmetric convective pattern as evidenced by multiple observational (e.g., Chen *et al.*, 2006; Corbosiero & Molinari, 2002; DeHart *et al.*, 2014; Marks *et al.*, 1992; Stevenson *et al.*, 2016) and modeling (e.g., Finocchio & Rios-Berrios, 2021; Frank & Ritchie, 1999) studies. In general, a TC usually intensifies after the inner core becomes highly symmetric (e.g., Miyamoto & Takemi, 2013; Nolan *et al.*, 2024; Onderlinde & Nolan, 2016; Rios-Berrios *et al.*, 2018; Zawislak *et al.*, 2016) which often occurs simultaneously with tilt reduction (Schecter, 2022). Observations have found that the azimuthal coverage of precipitation is greater for intensifying storms versus steady state (Rogers *et al.*, 2013).

The combined effect of wind shear and dry air has been studied through ventilation, defined as the flux of low-θ_e environmental air into the TC center (Simpson and Riehl Simpson *et al.*, 1958; Riemer *et al.*, 2010; Tang & Emanuel, 2012a). Low-θ_e air works against the TC heat engine and stunts development by reducing the thermodynamic efficiency and the work available to sustain the TC against friction (Cram *et al.*, 2007; Marín *et al.*, 2009; Munsell *et al.*, 2013; Tang & Emanuel, 2010, 2012b; Yu *et al.*, 2023). This ventilation can come from downdrafts (Alland *et al.*, 2021a; Riemer *et al.*, 2010; Wadler *et al.*, 2023) or mid-level, radial ventilation (Alland *et al.*, 2021b; Tang & Emanuel, 2010). To look more closely at the wind shear and moisture effects on ventilation, Alland *et al.* (2021a, b) simulated nine TCs with low, medium, and high combinations of shear and moisture. TCs intensified quicker with higher humidity regardless of shear, but larger shear values ultimately stunted growth (Alland *et al.*, 2021a, b). For the same shear value, the tilt of the vortex was found to be controlled by the humidity, with larger initial tilt in drier environments. Stronger downdraft ventilation was discovered in weaker TCs embedded in higher shear and drier air, which resulted in the downward transport of low-θ_e air and reduction of the areal extent of the updrafts leading to less intensification of the vortex (Alland *et al.*, 2021a). The combined effect of lower troposphere radial ventilation of low-θ_e air left of shear and mid- and upper-tropospheric low-RH air right of shear inhibited convection and the secondary circulation, once again limiting the extent of the updrafts (Alland *et al.*, 2021b; Corbosiero & Molinari, 2002). Differences in RI timing of ensemble members of hurricane *Gonzalo* (2014) showed that late RI members had greater mid- to upper-tropospheric ventilation and were linked to a more tilted vortex (Fischer *et al.*, 2023). Many other studies have found that the combination of shear and dry air is most detrimental on the intensification of weak TCs (e.g.,

1477870x, 0, Downloaded from https://rmets.onlinelibrary.wiley.com/doi/10.1002/qj.5011 by University Of Miami - Law, Wiley Online Library on [22/08/2025]. See the Terms and Conditions (https://onlinelibrary.wiley.com/terms-and-conditions) on Wiley Online Library for rules of use; OA articles are governed by the applicable Creative Commons License

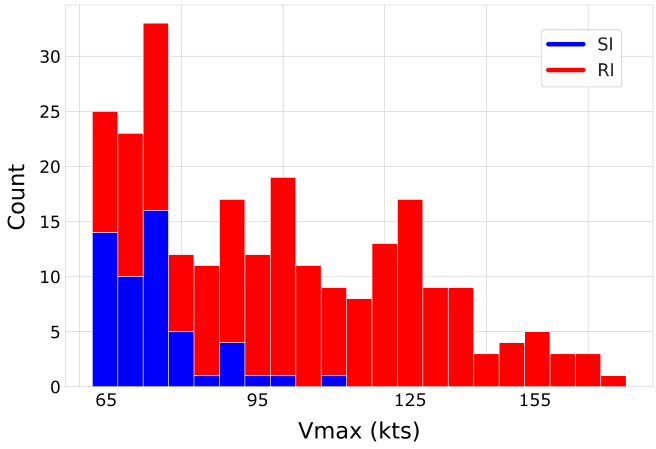


FIGURE 1 Frequency of the lifetime maximum intensity of all Atlantic hurricanes between 1980 and 2023 that underwent a maximum intensification rate of at least rapidly (RI) (30 kts·24 hr^{-1}; red) or less than or equal to slowly (SI) (20 kts·24 hr^{-1}; blue). Data from HURDAT (Landsea & Franklin, 2013). RI cases are stacked on top of SI cases. [Colour figure can be viewed at wileyonlinelibrary.com]

Rios-Berrios & Torn, 2017; Tang & Emanuel, 2012a; Tao & Zhang, 2014) but can also weaken TCs near the end of intensification (Finocchio & Rios-Berrios, 2021; Tang *et al.*, 2024).

The thermodynamic environment, mainly temperature and moisture, is usually prescribed by the Dunion (2011) moist tropical sounding, that was compiled from the average observations of four Caribbean stations between 1995 and 2002 from July to October. Whilst these profiles are a good example of a tropical thermodynamic profile during the North Atlantic hurricane season, they do not encompass the entire Atlantic, nor are they TC-relative. In regard to shear, many idealized modeling studies have focused on varying its magnitude, height, or depth (e.g., Finocchio *et al.*, 2016; Finocchio & Majumdar, 2017; Finocchio & Rios-Berrios, 2021; Tao & Zhang, 2015). Storms in these studies usually intensify through RI when the shear is below a certain threshold or fail to intensify at all if above (Tao & Zhang, 2015; Yu *et al.*, 2023). Whilst the field has advanced in its understanding of the factors that contribute to RI, the nuances behind slower intensifying storms have not been widely addressed. Figure 1 shows that whilst the vast majority of major hurricanes experience RI, there are still a considerable number of hurricanes that only intensify by at most 20 kts·24 hr^{-1}. This bimodal distribution of the lifetime maximum intensity of TCs, where one peak corresponds to slower intensifiers and another for RI, has been shown previously (Lee *et al.*, 2016). This demonstrates the need to model slower intensifying tropical cyclones to better distinguish them from rapidly intensifying storms by using TC-relative environmental profiles, as obtained by Nebylitsa *et al.* (2023). By using these profiles, for the first time to the authors' knowledge, simulations will include both rapidly and *slowly* intensifying TCs. This will lead to additional insights into the structure and thermodynamics of TCs in an idealized framework that exemplifies the real world more closely than before.

The environmental profiles and model configuration will be explained in Section 2. Section 3 will describe the evolution of the environment and storm intensity. Storm structure will be evaluated in Section 4 and ventilation in Section 5. Concluding remarks are presented in Section 6.

2 | METHODS

2.1 | Environmental profiles

In idealized models, a simplified 850–200-hPa westerly shear profile, where the wind below 850 hPa and above 200 hPa is the same as that level, commonly only considers the zonal wind component. Between 850 and 200 hPa, the zonal wind usually follows a sinusoidal function (e.g., Finocchio *et al.*, 2016) or increases linearly with height (e.g., Alland *et al.*, 2021a). The commonly used moisture profile is Dunion (2011), and any adjustments to the moisture are made relative to this profile. To provide a more accurate representation of the evolution of idealized TCs, it is important to use profiles that are consistent with the environment around TCs, as in Finocchio and Majumdar (2017). For different annuli and intensification rates, Nebylitsa *et al.* (2023) computed the average wind (u and v), temperature (T), and moisture (mixing ratio, q) profiles from the European Centre for Medium-Range Weather Forecast version 5 reanalysis (ERA5; Hersbach *et al.*, 2020) for all intensifying Atlantic TCs between 1980 and 2021 for 23 vertical levels between 1000 and 100 hPa.

The wind shear calculated from the average u and v wind for all storms is not equal to the average of the wind shear over each event. In this study, we adjust the wind profiles such that the calculation of the 850–200-hPa wind shear yields the climatological average for the 200–800-km annulus from the TC center from Nebylitsa *et al.* (2023): 6 m·s^{-1} for RI and 8.6 m·s^{-1} for slow intensification (SI, 5–10 kts·24 hr^{-1}). An example of this adjustment process is shown in Figure 2a, where the blue dashed line represents the averaged u wind for all slowly intensifying events in the climatology. Following the methodology in McGauley and Nolan (2011), Empirical Orthogonal Function (EOF) analysis is conducted and the first EOF for the u wind is shown in the blue dotted line (Figure 2a). This EOF is multiplied by a factor such that when the modulated EOF is added to the original averaged wind profile, the new wind profile yields the desired 850–200-hPa shear

1477870x, 0, Downloaded from https://rmets.onlinelibrary.wiley.com/doi/10.1002/qj.5011 by University Of Miami - Law, Wiley Online Library on [22/08/2025]. See the Terms and Conditions (https://onlinelibrary.wiley.com/terms-and-conditions) on Wiley Online Library for rules of use; OA articles are governed by the applicable Creative Commons License

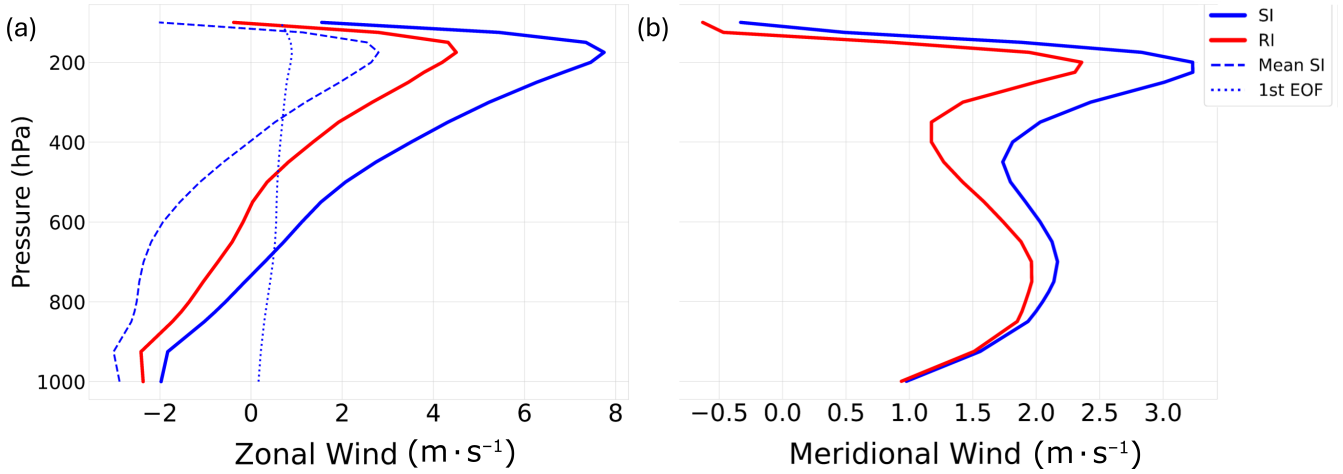


FIGURE 2 Adjusted wind profiles for rapidly (RI) (red) and slowly (SI) intensifying (blue, solid) (a) zonal and (b) meridional winds. Original averaged zonal winds for SI are shown in a dashed blue line with the first empirical orthogonal function (EOF) in a dotted blue line. [Colour figure can be viewed at wileyonlinelibrary.com]

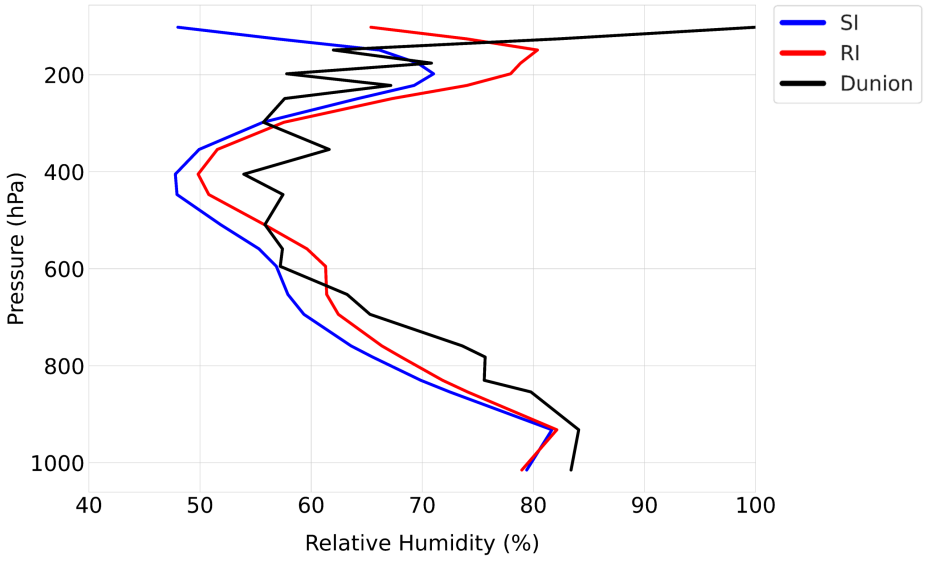


FIGURE 3 Calculated relative humidity for rapidly (RI) (red), and slowly intensifying (SI) (blue) storms, and Dunion (black). [Colour figure can be viewed at wileyonlinelibrary.com]

value. The addition of the EOF to the zonal wind profiles yields larger upper-level westerlies, displayed in the solid lines in Figure 2a, resulting in an eastward-moving TC. Thus, the wind profiles are shifted 5 m·s^{-1} to the west to ensure realistic westward TC motion in the main development region within the idealized simulation, by increasing low-level easterlies. This reduces the unrealistically large upper-level wind magnitudes. The EOF adjustment is also applied to the meridional winds and their result is displayed in Figure 2b. The adjusted zonal and meridional winds at the 23 vertical levels are presented in the Appendix (Table A1).

Relative humidity is calculated with respect to ice above the freezing level from the average climatological T and q (Table A1) for all RI and SI events in a 200–800-km annulus and is compared to the Dunion (2011) profile (Figure 3). From the surface to about 300 hPa, the Dunion profile is usually moister than both the RI and SI profiles. The only layer in which the Dunion profile falls within the RI and SI profile is between 500 and 700 hPa. This is, coincidentally, the mid-tropospheric layer that has historically been used in TC-relative environment studies (e.g., Hendricks *et al.*, 2010). This demonstrates that while the Dunion sounding may accurately represent the Atlantic mid-troposphere, the use of a TC-relative area and additional regions outside the Caribbean, such as the tropical east Atlantic, results in a drier atmosphere that is still conducive to TC intensification. The large differences in the calculated humidity at the 100- and 125-hPa levels are a result of the averaged q values from ERA5 being an order of magnitude smaller than in Dunion. This may be possibly due to inherent differences in reanalysis data and rawinsondes and generally low moisture in the upper troposphere.

1477870x, 0, Downloaded from https://rmets.onlinelibrary.wiley.com/doi/10.1002/qj.5011 by University Of Miami - Law, Wiley Online Library on [22/08/2025]. See the Terms and Conditions (https://onlinelibrary.wiley.com/terms-and-conditions) on Wiley Online Library for rules of use; OA articles are governed by the applicable Creative Commons License

2.2 | Model configuration

All simulations are produced using version 4.3.3 of the Weather Research and Forecasting Model (WRF; Skamarock *et al.*, 2019). The model is configured with 60 vertical levels between the surface and $z = 20$ km, using the vertical distribution of Nolan *et al.* (2013). Since the 100-hPa data only reach a geopotential height of 16.5 km, the profiles are set constant above that level. The sea surface temperature is 28°C on a doubly periodic f-plane at 20° N. A vortex-following nested grid is used. The outer domain has a resolution of 18 km with 312 × 312 grid points, the first nested domain has a resolution of 6 km and 204 × 204 grid points, and the second nest has a resolution of 2 km with 336 × 336 grid points. The Yonsei University boundary layer scheme (YSU; Hong *et al.*, 2006), Morrison microphysics scheme (Morrison *et al.*, 2005, 2009), and the Tiedtke cumulus parameterization scheme, only on the parent domain, (Tiedtke, 1989; Wang *et al.*, 2007) are used. A simple mixed layer ocean model with a mixed layer depth of 10 m and a lapse rate of 0.1 K·m^{-1} is used to achieve ocean cooling (Zarzycki, 2016). The RRTMG longwave and shortwave radiation schemes are used (Iacono *et al.*, 2008). Simulations are run for eight days, with a start date and time of 1 September 0000 UTC for radiative purposes.

The time-varying point-downscaling (TVPDS) method (Onderlinde & Nolan, 2017) allows the environmental u and v winds, T, and q in the outermost domain to be nudged to a specified profile that can also change with time. TVPDS uses both a nudging interval, t, the transition time between environments, and a nudging time scale (relaxation rate), τ, such that:

$$\frac{du(z)}{dt} = -\frac{1}{\tau}[u(z) - u_n(z,t)], \tag{1}$$

where, for example, $u(z)$ is the zonal wind at level z and $u_n(z,t)$ is the prescribed nudging value at level z at time t. For larger values of t and τ, it takes longer for the environment to fully transition between profiles. The u and v winds, T, and q are all nudged over 18 hours (t) with a six-hour relaxation rate (τ).

An initial vortex is created with a maximum intensity (V_{max}) of 20 m·s^{-1} (38.9 kt) and an RMW of 90 km. Five ensemble members made from random perturbations to the initial wind field are used to create an RI and SI ensemble from the RI and SI environmental profiles, respectively. The evolution of the environmental variables is shown in Figure 4. At $t = 0$, the zonal wind is at a constant −5 m·s^{-1} and there is no meridional wind. Additionally at $t = 0$, the T and q profiles are that of the RI case. Over the first 18 hours, the shear increases to 15 m·s^{-1}, with a zonal profile that follows a cosine function, and the RI T and q profiles remain. During the subsequent 18 hours, the shear relaxes to the RI or SI profiles and for the SI ensemble, to the SI T and q. Since the values of T and q for the RI and SI profiles are nearly identical, they are not shown in Figure 4. Rather, the difference between the RI and SI T and q are plotted to indicate the use of the respective thermodynamic profiles with their wind profiles (Figure 4; post 18 hours). The RI and SI environmental profiles are continuously nudged onto the parent domain for the remainder of the eight-day simulation.

2.3 | Model justification

Extensive testing within the model environment was undertaken to ensure that the RI and SI ensemble underwent their respective intensification rates. This included a lower initial V_{max} and lower SST. TCs were also allowed to spin up before the RI and SI profiles were introduced through various forcing times (t and τ). Despite the SI shear value of 8.6 m·s^{-1} being larger than the threshold value of 7.5 m·s^{-1} found in previous studies prohibiting intensification (Tao & Zhang, 2015; Yu *et al.*, 2023), intensifying storms in the SI environment still underwent RI. This demonstrates that the specific model environment can be a key influence on whether a storm intensifies or not. Due to the consistent RI in the SI environment, radiation and ocean cooling were included in the model configuration to reduce lifetime V_{max} and consequently the storms' maximum intensification rate. Radiative processes have been found to affect several aspects of TCs such as earlier intensification (Chen *et al.*, 2023; Rios-Berrios, 2020), lower lifetime maximum intensity (Ruppert *et al.* Ruppert Jr *et al.*, 2020; Chen *et al.*, 2023; Dai *et al.*, 2023), and increased predictability (Rios-Berrios, 2020). Introducing ocean feedback in the model can also affect intensification as TC-induced cold wakes have a negative effect on TC intensity (Chen *et al.*, 2010). We note that we use a single SST value of 28°C for both the RI and SI ensemble and that the use of different SSTs for each case could modify the results. However, during model testing, many SST values were used, but they did not produce appreciably different storm evolution as compared to shear and humidity. We did not see a reduction in intensification rates until the SST was reduced below 27°C.

Furthermore, the initial vortex is subjected to a period of strong (15 m·s^{-1}) shear as shown in Figure 4. The gradual increase in shear allows the vortex to slightly intensify in the first day, so that it is not severely weakened when the stronger shear arrives. The shear results in strong asymmetries formed naturally between the vortex and its environment. This contrasts with those included at initialization

1477870x, 0, Downloaded from https://rmets.onlinelibrary.wiley.com/doi/10.1002/qj.5011 by University Of Miami - Law, Wiley Online Library on [22/08/2025]. See the Terms and Conditions (https://onlinelibrary.wiley.com/terms-and-conditions) on Wiley Online Library for rules of use; OA articles are governed by the applicable Creative Commons License

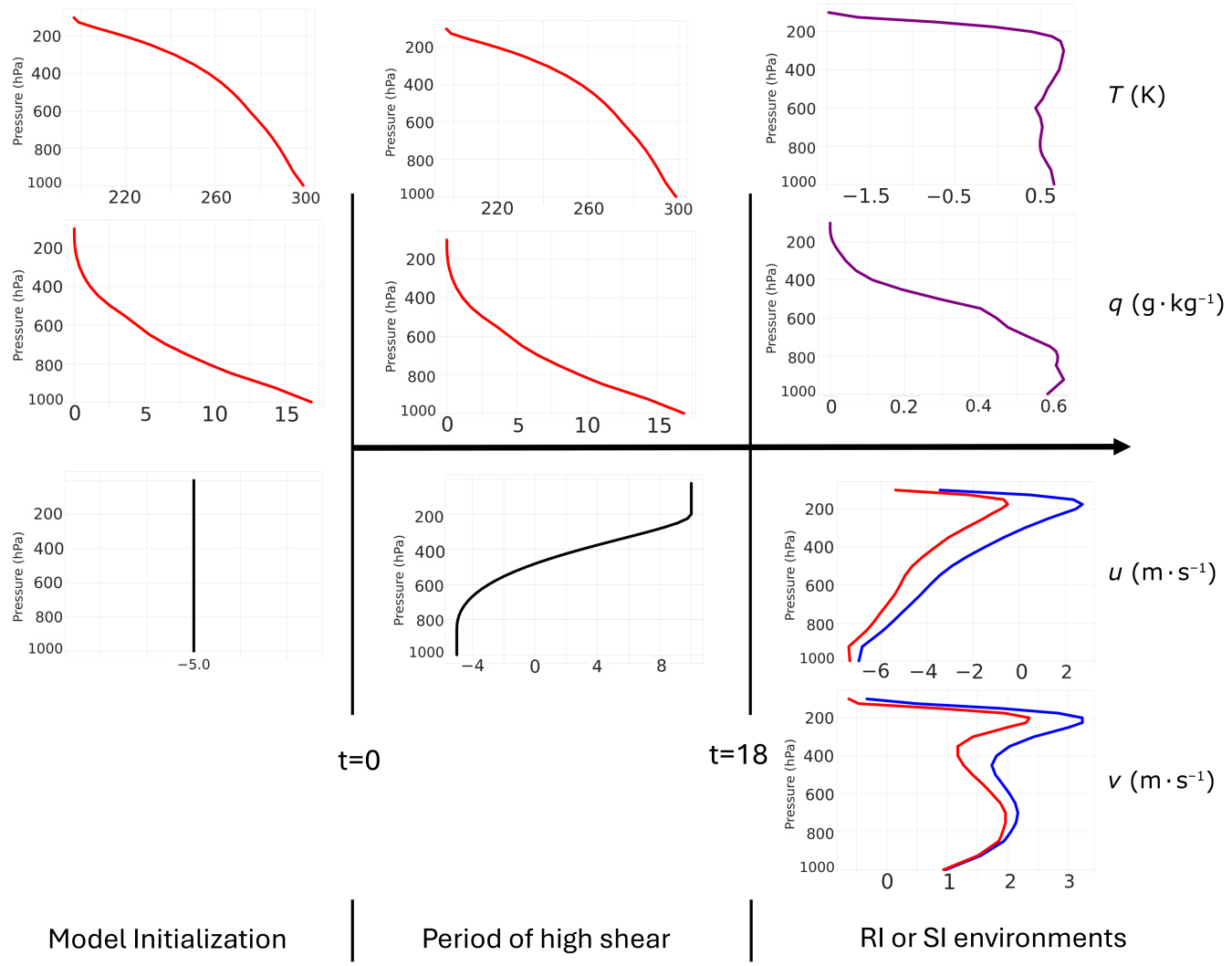


FIGURE 4 Timeline showing the evolution of the wind, below the line, and T and q above the line. At $t = 0$, model initialization, there is no wind shear and T and q are the more favorable rapidly intensifying (RI) conditions (red). Between $t = 0$ and $t = 18$, the shear transitions to 15 m·s^{-1}, but the RI T and q remain. After hour 18, the wind and environment follow either the RI or slowly intensifying (SI) (blue) profiles. T and q post $t = 18$ are plotted in purple to indicate the difference between RI and SI as described in the text. The zonal wind displayed here is shifted 5 m·s^{-1} to the west from Figure 2a. [Colour figure can be viewed at wileyonlinelibrary.com]

in Nolan *et al.* (2024) that have only been shown to delay, not prevent RI. The initial shearing of the TC, in conjunction with the added radiative and ocean cooling effects, allowed for the storm in the SI environment to not undergo RI. While the SI storms still undergo a modest intensification rate of about 20 kts 24 hr^{-1}, this was near the lower end of what could be achieved within the model without pushing it to unrealistic configurations. We recognize that this "new" SI rate is considerably larger than the SI rate used to define the environmental profiles. However, as shown in Figure 1, several TCs reached hurricane status via this intensification rate, and thus the SI ensemble would be representative of them. We also acknowledge that there is a large range of shear values outside of those prescribed here that result in RI and SI (Nebylitsa *et al.*, 2023 and references therein). There are additional factors in the real world that influence intensification rates outside of shear, including but not limited to, the non-uniformity of the environment and land masses.

3 | INTENSITY AND ENVIRONMENT EVOLUTION

The TC center is computed by taking the centroid of the smoothed negative pressure anomaly, similar to the methods of Nguyen *et al.* (2014). V_{max} is computed as the single largest 10-m wind speed value on the 6-km grid, within 120 km from the storm center, to exclude any large wind values in strong rainbands further from the

1477870x, 0, Downloaded from https://rmets.onlinelibrary.wiley.com/doi/10.1002/qj.5011 by University Of Miami - Law, Wiley Online Library on [22/08/2025]. See the Terms and Conditions (https://onlinelibrary.wiley.com/terms-and-conditions) on Wiley Online Library for rules of use; OA articles are governed by the applicable Creative Commons License

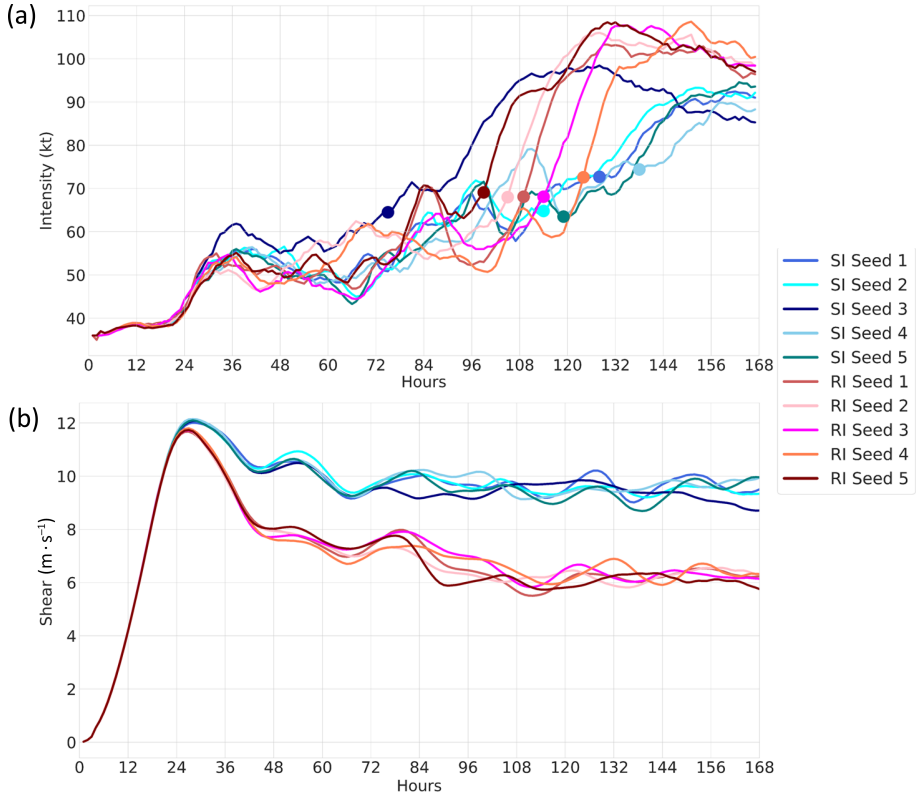


FIGURE 5 Six-hourly smoothed (a) maximum intensity (V_{max}), (b) 200–800-km 850–200-hPa shear for the slowly (SI) (cool colors) and rapidly intensifying (RI) (warm colors) ensemble for the first seven days of the simulation. Points represent the designated onset times. [Colour figure can be viewed at wileyonlinelibrary.com]

TABLE 1 Maximum intensification rates and their designated onset times as defined in the text for each ensemble member for RI/SI (SI is italicized).

	Seed 1	Seed 2	Seed 3	Seed 4	Seed 5
Max intensification rate (kts·24 hr^{-1})	45/*18*	44/*22*	47/*27*	43/*15*	34/*24*
Onset time (hr)	109/*128*	105/*114*	114/*75*	124/*138*	99/*119*

center. A moving six-hourly average of V_{max} is calculated to emulate the official six-hourly analysis from the National Hurricane Center (Landsea & Franklin, 2013) (Figure 5a).

Figure 5 shows the effect of the 15 m·s^{-1} shear on the vortex, with slight intensification followed by some weakening. The shear increases over the first 18 hours, but it does not reach its maximum in the 200–800-km environment until hour 24 and with only a magnitude of 12 m·s^{-1} (Figure 5b). The six-hour relaxation timescale and the nudging scheme prohibits the environmental shear from reaching the maximum value. Furthermore, the 6-km grid accounts for the majority of the 200–800-km annulus where the environmental shear is calculated. Since the environment is only nudged on the parent domain, there is additional delay in the nested domains' response. This is evident as the TC is still intensifying until hours 30–36, depending on the ensemble member, after which some weakening occurs and persists until about hour 72 (Figure 5a). Around this time, the shear reaches a quasi-steady minimum value at, or just slightly above, the prescribed shear (Figure 5b). Most ensemble members undergo their maximum intensification between 96 and 144 hours of the simulation (Table 1). There is a considerable difference in the intensification of RI (warm colors) and SI (cool colors) events (Figure 5a), with an average difference in maximum intensification rates of 20 kts 24 hr^{-1} (Table 1). The stronger shear and slightly drier atmosphere in SI compared to RI have successfully translated to two different intensity evolutions that can be studied further.

The random perturbations in the initial wind field result in similar maximum rates of intensification, but at different times. One SI member, Seed 3, intensifies earlier and at a much higher maximum rate, which may be partially explained by its overall higher intensity through the shearing and reorganization process as compared to all other members. One RI member, Seed 5, intensifies at a considerably lower rate, just barely qualifying as RI, experiencing a brief steady-state period at hour 108, which disrupts the intensification and results in a lower maximum intensification rate. Results in the remaining sections of

1477870x, 0, Downloaded from https://rmets.onlinelibrary.wiley.com/doi/10.1002/qj.5011 by University Of Miami - Law, Wiley Online Library on [22/08/2025]. See the Terms and Conditions (https://onlinelibrary.wiley.com/terms-and-conditions) on Wiley Online Library for rules of use; OA articles are governed by the applicable Creative Commons License

this paper will be considered relative to the onset time of RI or SI and are defined as follows and presented in Table 1. For the purposes of analysis, the onset of RI is the start of the largest six-hourly increase in V_{max} within the RI period, occurring slightly after the visual "kink" in the intensity plot as noted by the points in Figure 5a. This allows for a more accurate RI onset time as it removes the possibility of considering a period where the storm was relatively steady state for a few hours before intensifying, even though it reaches the RI qualification. For the SI onset, the 24-hour intensification rate was calculated for each hour. The onset time was designated as the first observed increase in intensity of at least 20 kts in 24 hours. For those cases that did not achieve at least a 20 kt increase, the onset time was the start of their respective largest intensification rates (Seeds 1, 4). Several RI and SI members undergo an earlier period of moderate intensification followed by a period of almost equal weakening. For consistency, the analyzed periods are those leading up to the storm's maximum intensity. This specific designation of the onset times for both RI and SI allows for better discrimination between the two ensembles as we consider the most rapid increase in V_{max} as onset of RI and a considerably slower increase in V_{max} as onset of SI.

4 | STORM STRUCTURE

4.1 | Tilt

Storm vertical tilt between the surface and 6 km is calculated by finding the centroid of the sign-preserved square of the vorticity following Nolan *et al.* (2024) within a 200 × 200 km box around the surface center. The six-hourly running average of tilt for each of the ensemble members as well as the ensemble mean is shown in Figure 6 for a two-day period centered around the onset time. From the ensemble mean, the RI ensemble has a larger tilt in the day prior to onset compared to the SI ensemble but decreases to a smaller tilt around six hours prior to onset and remains smaller after the onset time. The larger tilt in some RI ensemble members can be attributed to a more expansive upper-level convective area (not shown), resulting in the 6-km vorticity centroid being slightly further from the surface center as compared to the SI ensemble members. Individually, at onset, three of the five RI members have the smallest tilt, and three of the five SI members have the largest, with the two remaining members from each ensemble having an almost identical tilt in between. From the Welch's *t*-test, the two ensembles are significantly different from each other at the 95% level starting at hour 3 post onset and at the 93% level at onset, demonstrating that the slightly larger tilt in the SI cases through the intensification process is significant.

Even though on average the RI ensemble has a smaller tilt at onset compared to SI, there is still considerable variability amongst the individual members, indicating that a smaller tilt is not necessarily followed by a larger intensification rate. The two SI members with the smallest tilt at onset also have the lowest tilt a day prior, so potentially, it is the change in tilt and rapid vertical alignment that preludes RI versus a slower intensification. Variance is computed from the unsmoothed tilt magnitudes of each ensemble member in a six-hourly moving window and averaged to produce the mean ensemble variability in tilt (not shown). Between 12 and 6 hours pre onset, the RI ensemble mean variance is 80 km, decreasing to near 0 km at onset, and Figure 6 demonstrates this rapid decrease in tilt in the RI ensemble mean compared to the SI ensemble mean. Another notable difference between the RI and SI ensemble tilt variability is evident during the intensification process. Whilst the ensemble mean shows that SI does maintain a larger tilt than RI post onset (Figure 6), both are quite low. However, the RI ensemble members converge towards the mean whereas the SI ensemble members' tilt is much more variable, suggesting that a more

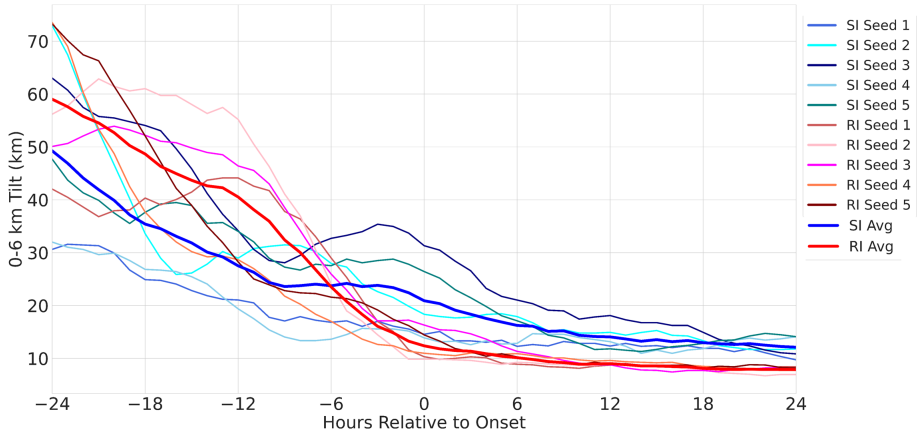


FIGURE 6 Six-hourly smoothed surface to 6-km tilt relative to the onset time for each ensemble member, colors as in Figure 4, and ensemble mean tilt for rapidly (RI) (red) and slowly intensifying (SI) storms (blue). [Colour figure can be viewed at wileyonlinelibrary.com]

1477870x, 0, Downloaded from https://rmets.onlinelibrary.wiley.com/doi/10.1002/qj.5011 by University Of Miami - Law, Wiley Online Library on [22/08/2025]. See the Terms and Conditions (https://onlinelibrary.wiley.com/terms-and-conditions) on Wiley Online Library for rules of use; OA articles are governed by the applicable Creative Commons License

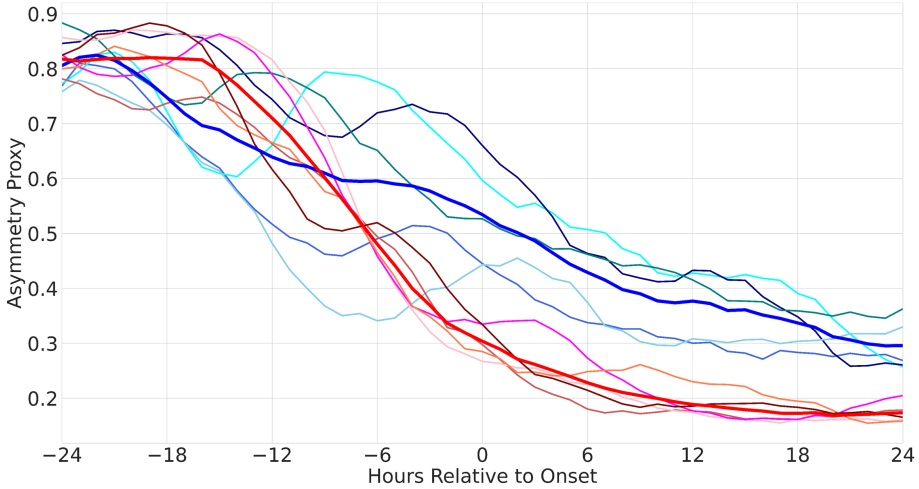


FIGURE 7 Six-hourly smoothed asymmetry parameter (γ). Colors as in Figure 6. [Colour figure can be viewed at wileyonlinelibrary.com]

consistent tilt is favorable for larger intensification rates. The rapid alignment in the RI members a few hours prior to onset was also shown in the "marathon" RI mode of Judt *et al.* (2023).

4.2 | Asymmetry

Studies have shown that environmental and mesoscale asymmetries can delay TC intensification (Nolan *et al.*, 2024), and intensification commences once the storm reaches an axisymmetric state (Miyamoto & Nolan, 2018; Rios-Berrios *et al.*, 2018). Following Miyamoto and Takemi (2013) and Rios-Berrios *et al.* (2018) we develop our own asymmetry parameter based on simulated reflectivity (dBZ), averaged between $z = 1$–2 km and $r = 20$–80 km:

$$\gamma_{(r,z,t)} = \frac{\overline{|\, X'(r,\lambda,z,t)\,|}}{\overline{X}(r,z,t)}, \tag{2}$$

where X' denotes the perturbation from the azimuthal mean, $\overline{X}$, of reflectivity. A highly symmetric storm would exhibit minimal perturbations from the azimuthal mean, producing a smaller γ, whereas a very asymmetric storm would contain large perturbations, and thus, a larger γ. The RI ensemble displays a much lower γ than the SI ensemble post onset (Figure 7) and the two are significantly different at the 95% level starting at four hours pre onset. Prior to −4 hours, the RI and SI members have overlapping asymmetry parameter distributions (Figure 7). As was observed for tilt, the RI ensemble does boast a higher average γ until about nine hours pre onset and consequently the largest decrease in γ as well. This indicates that rapid symmeterization over 6–12 hours is a robust signal that indicates the onset of RI. It is also of note that there is less spread amongst the individual RI members compared to the SI members, revealing that the asymmetry evolution in RI storms is a clear signal (Figure 7). The fluctuations in tilt and asymmetry prior to onset in several SI members (2, 4, and 5) can be tied to the fluctuations in $V_{\max}$, such that local minima or maxima of tilt or asymmetry yield a short intensification or weakening period, respectively. Seed 4 has the highest correlation, at −85% for both tilt and asymmetry compared to intensity. Seeds 2 and 5 have a −65% correlation between tilt and intensity. This furthers the notion that larger variations in tilt and/or asymmetry can impede RI.

The asymmetry parameter also serves as a quantitative representation of the precipitation asymmetry as seen through the 1-km simulated reflectivity (Figures 8–11). This suggests that the method developed could be applied in real time to provide additional information on the storm structure. This calculation can be integrated into weather models, and observations from radars either on aircraft or land, if the storm is in range, can also be used to verify the method. At 24 hours pre onset, the majority of the convection is concentrated in the downshear left quadrant of the storm for all ensemble members (Figure 8). The black arrow indicates the average shear direction for all RI and SI ensemble members and deviates $\pm 10^{\circ}$ throughout the next 48 hours. At this time, it is impossible to distinguish the two intensification rates from each other, which is corroborated by both ensembles having an average γ value of 0.8. The spread of both ensembles is also very similar (Figure 7).

At 12 hours pre onset, convection has extended into the upshear left quadrant at least, with some ensemble members from both RI and SI attempting to create a closed eye and bring the convection around to the right-of-shear side (Figure 9). Two SI members have the lowest γ, 0.5, and this corresponds to the two images (Figure 9f,i) with the most defined eye. As in the tilt analysis, these are the two ensemble members with the lowest maximum

1477870x, 0, Downloaded from https://rmets.onlinelibrary.wiley.com/doi/10.1002/qj.5011 by University Of Miami - Law, Wiley Online Library on [22/08/2025]. See the Terms and Conditions (https://onlinelibrary.wiley.com/terms-and-conditions) on Wiley Online Library for rules of use; OA articles are governed by the applicable Creative Commons License

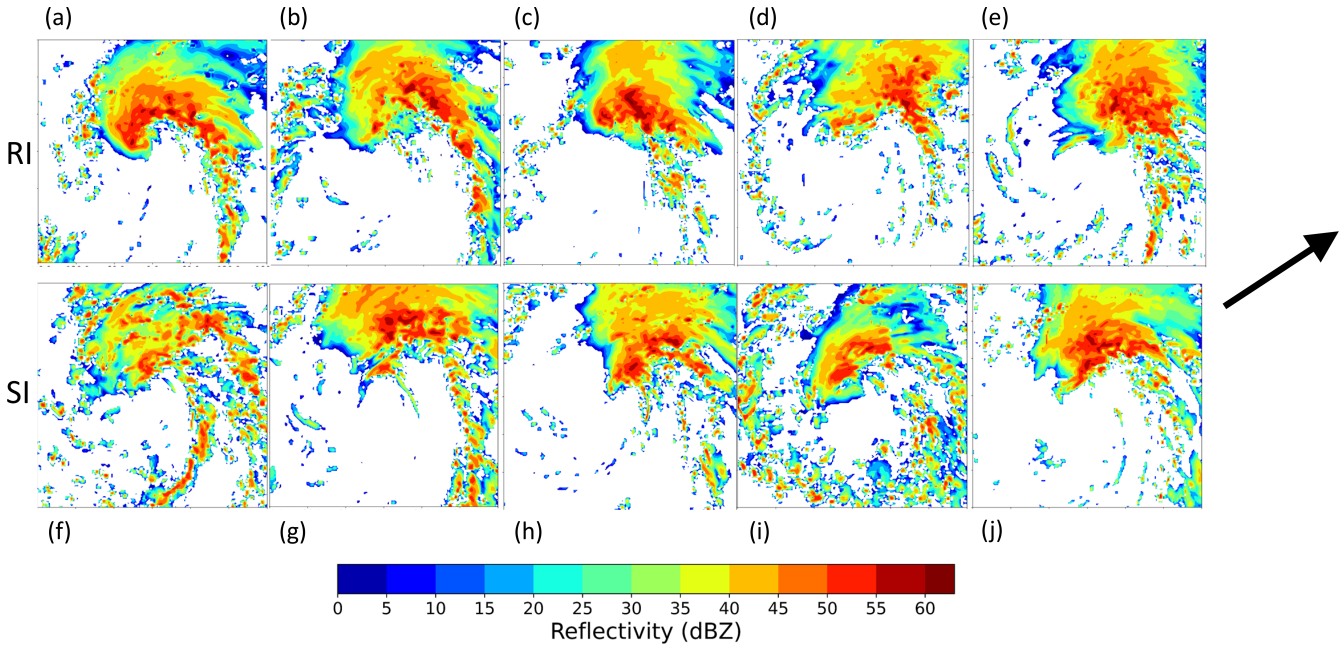


FIGURE 8 Simulated reflectivity at $z = 1$ km for all rapidly (RI) (a–e) and slowly intensifying (SI) (f–j) ensemble members 24 hours pre onset. Ensemble members are presented 1–5 from left to right. The black arrow indicates the average shear direction. All images are displayed in a 360 × 360 km storm-centered box. [Colour figure can be viewed at wileyonlinelibrary.com]

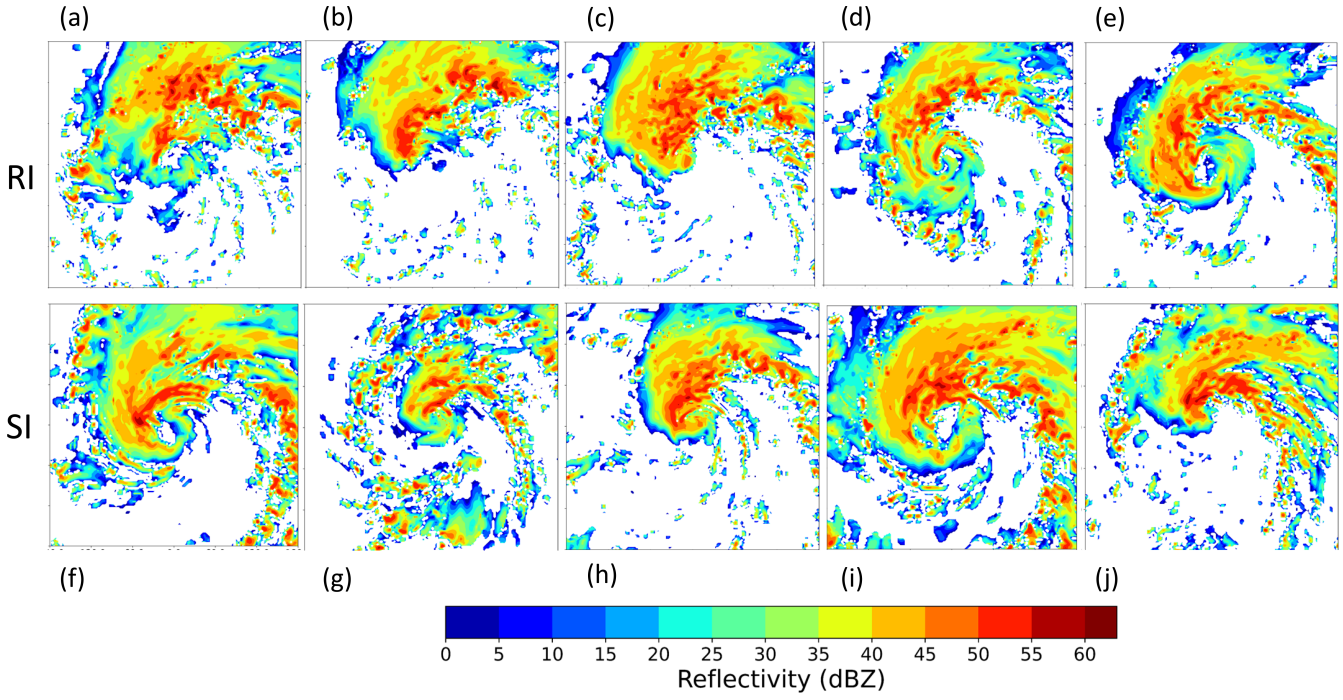


FIGURE 9 Same as Figure 8 except at 12 hours pre onset. [Colour figure can be viewed at wileyonlinelibrary.com]

intensification rate. The two RI members that have the largest γ correspond to the images (Figure 9b,c) where convection has yet to wrap around to the right-of-shear quadrant. It should be noted that at this time, the γ of the RI and SI ensembles are not statistically different from each other. Despite larger tilt and γ at −24 and −12 hours, the RI ensemble's average 34 kt 10-m wind radius, is 20–30 km smaller than for the SI ensemble, indicating a potentially more compact storm near the surface center. The RMW, around which γ is calculated, for all RI and SI ensemble members is not statistically different from each other at any point.

1477870x, 0, Downloaded from https://rmets.onlinelibrary.wiley.com/doi/10.1002/qj.5011 by University Of Miami - Law, Wiley Online Library on [22/08/2025]. See the Terms and Conditions (https://onlinelibrary.wiley.com/terms-and-conditions) on Wiley Online Library for rules of use; OA articles are governed by the applicable Creative Commons License

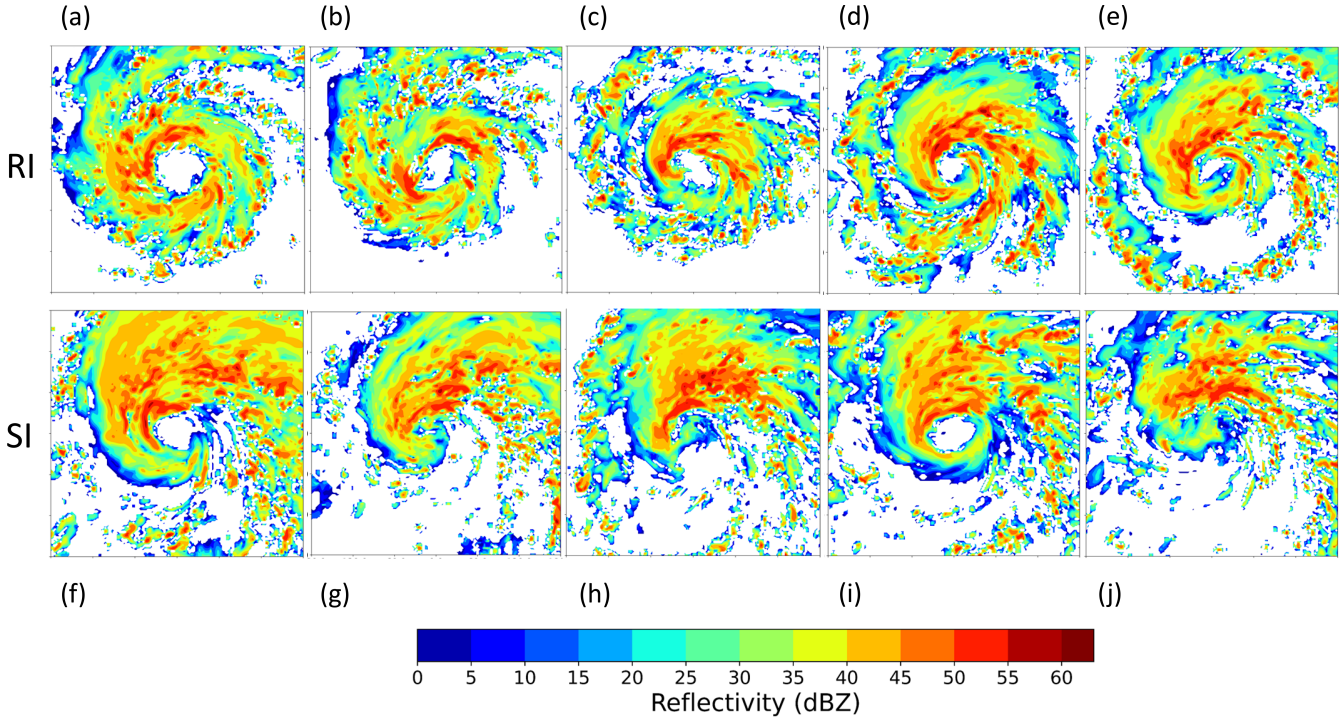


FIGURE 10 Same as Figure 8 except at onset. [Colour figure can be viewed at wileyonlinelibrary.com]

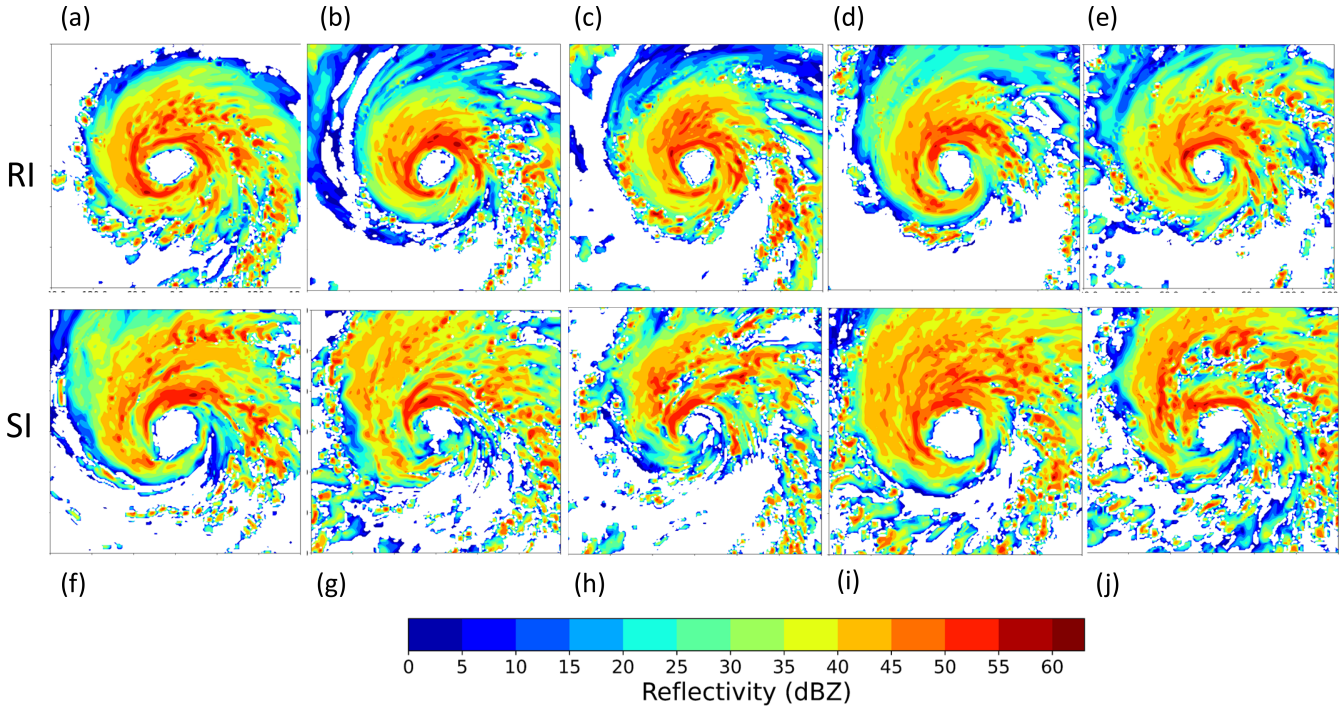


FIGURE 11 Same as Figure 8 except at 12 hours post onset. [Colour figure can be viewed at wileyonlinelibrary.com]

At onset, the RI average γ is considerably lower than the SI average (Figure 7). All RI members contain a visually apparent eye in the simulated reflectivity, whereas only the SI ensemble members that previously contained an eye have one (Figure 10). This causes the larger ensemble spread in the SI members as seen in Figure 7. Twelve hours into intensification, all ensemble members now show an eye (Figure 11), but the RI γ is still significantly lower than the SI γ. Calculating γ within a radius of 20–80 km from the TC center allows us to focus

1477870x, 0, Downloaded from https://rmets.onlinelibrary.wiley.com/doi/10.1002/qj.5011 by University Of Miami - Law, Wiley Online Library on [22/08/2025]. See the Terms and Conditions (https://onlinelibrary.wiley.com/terms-and-conditions) on Wiley Online Library for rules of use; OA articles are governed by the applicable Creative Commons License

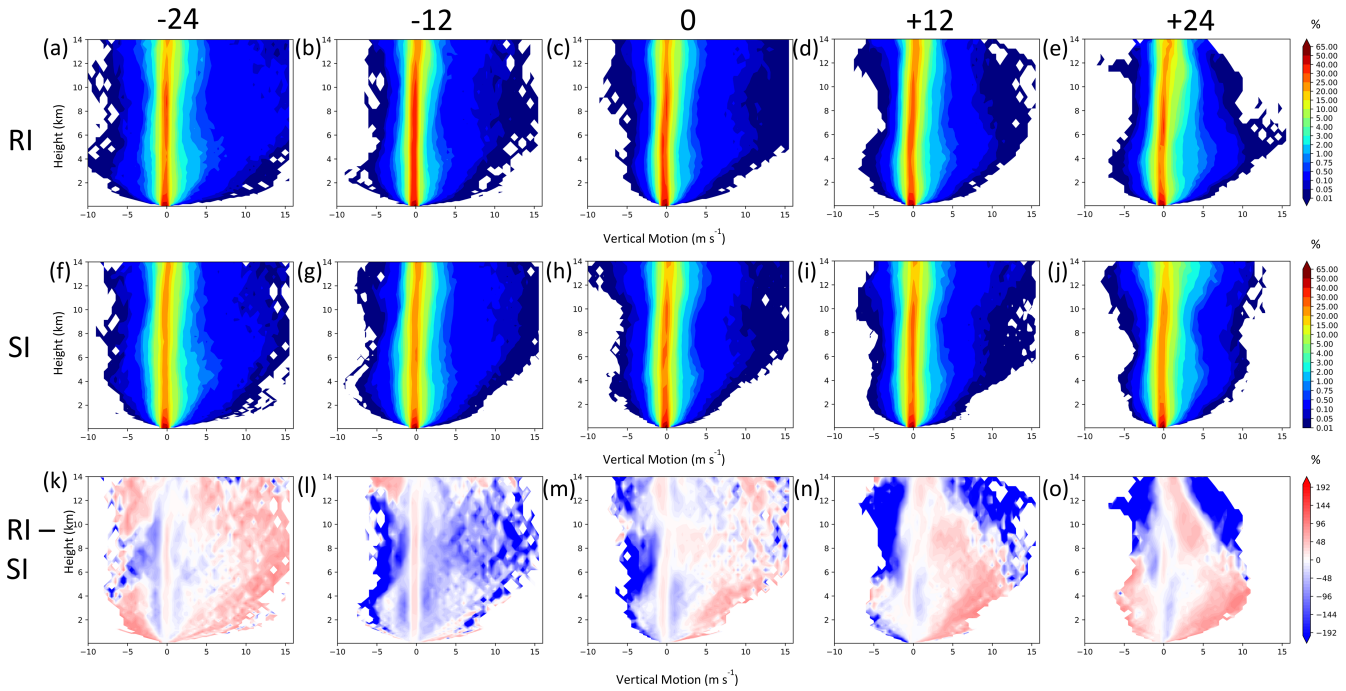


FIGURE 12 Ensemble composite contour frequency by altitude diagram (CFAD) of vertical velocity for rapidly (RI) (a–e), and slowly (SI) evolving storms (f–j), and percent change from RI to SI (k–o) for 24 hours pre onset (a,f,k), 12 hours pre onset (b,g,l), onset (c,h,m), 12 hours post onset (d,i,n) and 24 hours post onset (e,j,o). [Colour figure can be viewed at wileyonlinelibrary.com]

on the nuances of the inner core structure between the two ensembles. At first glance, storms in both ensembles appear organized, but at a closer look, the eyewall on the right-of-shear side in the SI ensemble is not always closed (Figure 11h). These small breaks and smaller radial coverage of the precipitation on the right-of-shear side result in a larger γ. All the RI members have a compact eye with similar azimuthal and radial coverage of precipitation around it.

Even though two SI members contain a visually apparent eye at 12 hours pre onset, it is the rapid symmeterization of the reflectivity within the subsequent 12 hours that preludes the onset of RI. The γ of those two SI members only decreased by about 0.05 whereas the RI γ decreased by 0.4 (Figure 7). Alvey III *et al.* (2015) also discovered increased rates of symmeterization of precipitation with increasing intensification rates from satellite data. This supports the idea that it is the time evolution of the storm structure, whether tilt, asymmetries, or otherwise, that provides the crucial information on the expected intensification of the storm. This was previously shown in the reanalysis study of Nebylitsa *et al.* (2023) when considering shear and relative humidity evolution relative to onset of different intensification rates. This may also help explain how the two RI ensemble members with the highest tilt are still able to undergo RI, including the largest intensification rate (RI Seed 3), and their counterpart SI ensemble members with similar tilt are not. Additional factors, such as ventilation (Section 5), may explain the lower intensification rates of the SI members despite their visual appearance.

4.3 | Vertical structure

To further investigate the vertical structure of the TCs, ensemble composite contour frequency by altitude diagrams (CFADs; Yuter & Houze Jr, 1995) for simulated reflectivity, in 5 dBZ bins, and vertical velocity, in 0.5 $m \cdot s^{-1}$ bins, are averaged within a 160×160 km box centered on the TC center (Figures 12 and 13). The CFADs for vertical velocity are calculated only where there was a sufficient reflectivity value, of 5 dBZ or more, to represent areas that could be sampled by radars, similar to Nolan *et al.* (2013). Since the vertical motion CFADs are plotted with a non-linear color bar, and the larger up- and downdrafts occur at very small percentages, the percent change between the RI (Figure 12a–e) and SI (Figure 12f–j) composites were calculated to extract differences between the two ensembles (Figure 12k–o). This also indicates that the majority of points occur at very small velocities (Figure 12a–j). At −24 hours, the percent change is maximized at the largest up- and downdrafts, indicating that RI cases tend to have more, larger, vertical

1477870x, 0, Downloaded from https://rmets.onlinelibrary.wiley.com/doi/10.1002/qj.5011 by University Of Miami - Law, Wiley Online Library on [22/08/2025]. See the Terms and Conditions (https://onlinelibrary.wiley.com/terms-and-conditions) on Wiley Online Library for rules of use; OA articles are governed by the applicable Creative Commons License

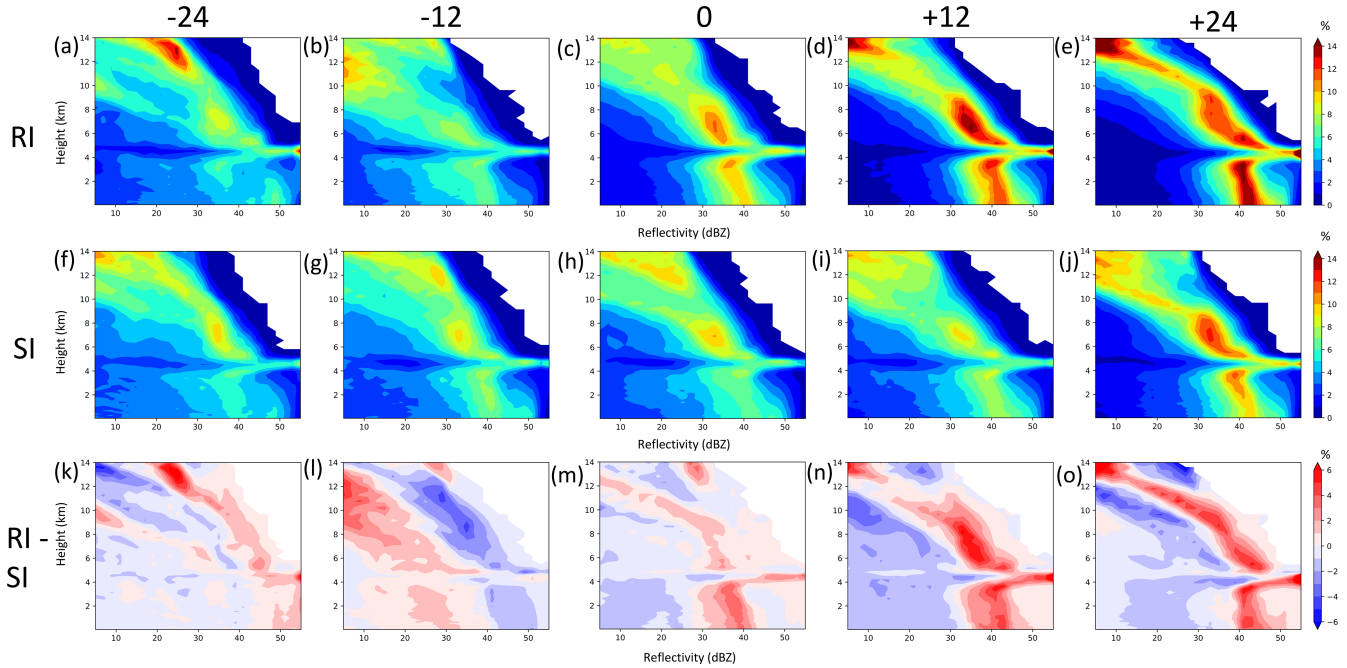


FIGURE 13 (a–j) Same as Figure 12, except for simulated reflectivity. (k–o) Rapidly (RI) – slowly intensifying (SI) storms at each respective time. [Colour figure can be viewed at wileyonlinelibrary.com]

velocities (Figure 12k; red shading). A small exception is seen around the melting layer where the SI ensemble has the largest downdrafts (blue shading). At −12 hours, the SI ensemble begins to have more downdrafts compared to the RI ensemble, and this remains through +12 hours (Figure 12l–n). Updrafts are also more frequent in the SI ensemble at −12 hours, but this does not follow the pattern at −24 hours and onset, where the RI ensemble has more updrafts. As a result, this time may be an outlier. At 12 hours, the SI ensemble begins to exhibit more upper-level updrafts that continue through hour 24 (Figure 12n,o). Concurrently, the RI ensemble begins to have a larger frequency of low-level downdrafts compared to SI.

From the reflectivity CFAD, the melting layer is clearly visible at all times in both ensembles at around 5 km altitude (Figure 13). Near the surface, the highest percentage of reflectivity occurs between 40 and 45 dBZ for all times presented and both ensembles. The only exception is the RI ensemble at −24 hours (Figure 13a) which has the highest percentage at the surface at 50 dBZ. A peak in percentage above the melting layer around 35 dBZ is also evident at all times for both ensembles, but it is stronger pre onset for the SI ensemble (Figure 13f,g) and post onset for the RI ensemble (Figure 13c–e). This peak also reaches higher into the atmosphere for the RI ensemble, peaking at 10 km 24 hours post onset (Figure 13e), but only at about 8 km for the SI ensemble at the same time (Figure 13j). The RI and SI CFAD difference plots (RI-SI; Figure 13k–o) show the differences between the two ensembles in more detail. For all times except 12 hours prior to onset (Figure 13l), the RI ensemble has more points of higher reflectivity, more than 40 dBZ below the melting layer and more than 30 dBZ above, whilst the SI ensemble has more at lower reflectivities. Leading up to onset (Figure 13k,m), the RI ensemble has a higher percentage of reflectivities around 30 dBZ at 14 km altitude, but post onset, the SI ensemble has higher percentages (Figure 13n,o). This may be connected to the increase in upper-level updrafts in the SI ensemble post onset (Figure 12n,o).

At −24 hours, the RI and SI ensembles are most similar, characterized by the difference CFAD having the most muted colors (Figures 12k and 13k), with some exceptions (upper-level reflectivity). From the asymmetry analysis, the storms are most identical at this stage, which may also explain why the CFADs are also very similar. As noted, −12 hours (Figure 13l) does not seem to follow the same pattern of the other times, and this is also partly true for the vertical velocity (Figure 12l). At this stage, there is a lot of variability in storm structure (Figure 9) that may be contributing to these differences in distribution. A more thorough investigation into the specific differences and impacts of microphysics on intensification is needed to address some of the variability.

1477870x, 0, Downloaded from https://rmets.onlinelibrary.wiley.com/doi/10.1002/qj.5011 by University Of Miami - Law, Wiley Online Library on [22/08/2025]. See the Terms and Conditions (https://onlinelibrary.wiley.com/terms-and-conditions) on Wiley Online Library for rules of use; OA articles are governed by the applicable Creative Commons License

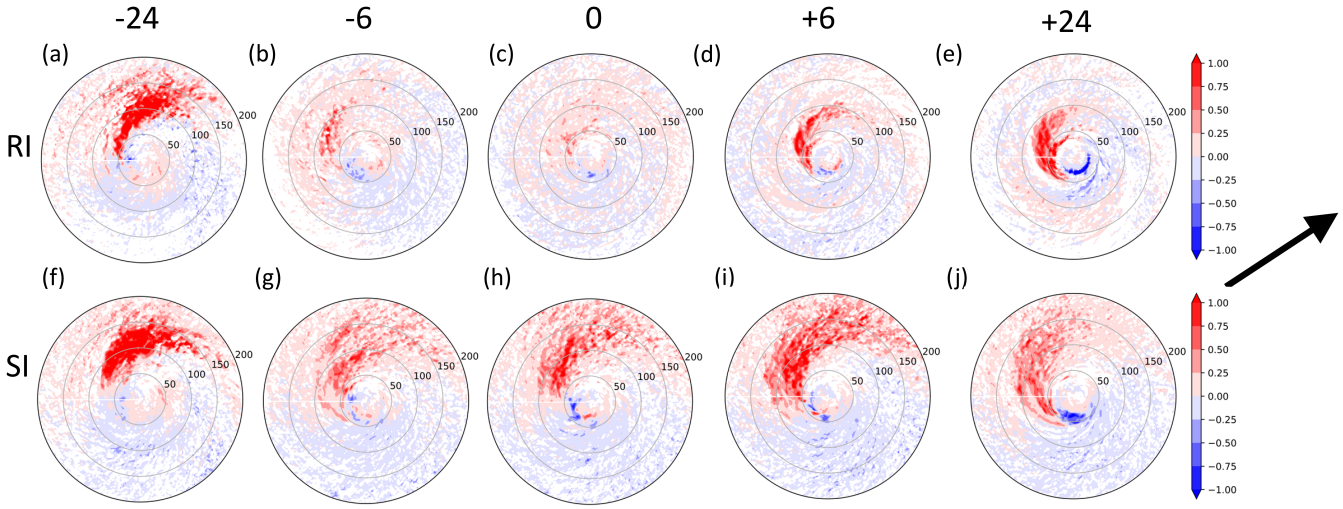


FIGURE 14 Ensemble averaged downdraft ventilation (kg·K·m^{-2} s^{-1}) at a height of 1 km for rapidly (RI) (a–e) and slowly (SI) intensifying storms (f–j) over a 6-hour period relative to 24 hours pre onset (a,f), 6 hours pre onset (b,g), onset (c,h), 6 hours post onset (d,i), and 24 hours post onset (e,j). The black arrow indicates the average shear direction. [Colour figure can be viewed at wileyonlinelibrary.com]

5 | VENTILATION

Downdraft ventilation is defined as $\rho w' \theta_e'$, where primes denote perturbations from the azimuthal mean. Downdraft ventilation was calculated at the 1-km level and only areas where there are downdrafts (< -0.1 m·s^{-1}) are plotted. A positive value (red shading) indicates downward transport of low-θ_e air (Alland *et al.*, 2021a; Riemer *et al.*, 2010). Ensemble mean of downdraft ventilation in six-hourly averaged intervals for RI and SI are plotted within 200 km of the TC surface center at select times (Figure 14). At a day prior to onset, both the RI and SI ensemble mean show a similar pattern of ventilation where the positive and negative values are separated roughly along the direction of the shear vector, presented in the black arrow, with downdraft ventilation appearing on the left-of-shear side (Figure 14a,f). Downdraft ventilation at −6 hours is maximized within the 50–100 km annulus in the upshear left quadrant but still extends out to 200 km in the downshear left for the SI ensemble but is only minimally present in the RI ensemble (Figure 14b,g). This decrease in downdraft ventilation for the RI ensemble continues until onset (Figure 14c), whereas it slightly increases for SI between −6 hours and onset (Figure 14h). Despite the increase in ventilation during RI (Figure 14d,e), the areal extent is still less than during SI (Figure 14i,j). The large decrease in ventilation prior to RI and the persistence of the ventilation in SI modulates the respective intensification rates. The increase in ventilation at +24 hours in the RI ensemble (Figure 14e), may help to explain the interruption of intensification and the weakening that occurs immediately after the RI period. Downdraft ventilation at −24 hours for each ensemble member is shown in Figure S1 in the supplementary material to demonstrate that whilst there is member-to-member variability, the ensemble mean extracts the key differences between the ensembles.

The corresponding six-hourly averaged ensemble mean of surface θ_e are plotted in Figure 15. At −24 hours, the surface θ_e for both ensembles are nearly identical, with the RI ensemble containing a larger area of the lowest θ_e values (Figure 15a,f). There is a large increase in the surface θ_e between −24 and −6 hours in the RI ensemble (Figure 15b), and less of an increase in the SI ensemble (Figure 15g). The θ_e at onset and through the intensification period for RI (Figure 15c–e) remains higher than that for SI (Figure 15h–j). This higher θ_e provides the necessary thermodynamic energy needed to achieve more rapid rates of intensification.

Radial ventilation, $\rho u' \theta_e'$, is calculated in a lower-atmosphere average (1–3 km; Figure 16) and upper-atmosphere average (5–9 km; Figure 17), where u is the storm relative radial velocity, representing the radial inflow of θ_e into the inner core (Tang & Emanuel, 2010). Only areas where there is inflow are plotted, and positive values indicate inward transport of low-θ_e air (Figures 16, 17). As in the downdraft ventilation, both the RI and SI ensemble mean show a similar pattern of radial ventilation a day prior to onset (Figures 16a,f and 17a,f). Between −24 hours and −6 hours, the ventilation decreases in both ensembles, but an area of greater radial ventilation is present in the SI ensemble between 150 and 200 km in the downshear left region (Figure 16b,g) that persists through +6 hours (Figure 16h,i). Additionally, there is a maximum of radial ventilation within 50 km in the downshear right region that remains through

1477870x, 0, Downloaded from https://rmets.onlinelibrary.wiley.com/doi/10.1002/qj.5011 by University Of Miami - Law, Wiley Online Library on [22/08/2025]. See the Terms and Conditions (https://onlinelibrary.wiley.com/terms-and-conditions) on Wiley Online Library for rules of use; OA articles are governed by the applicable Creative Commons License

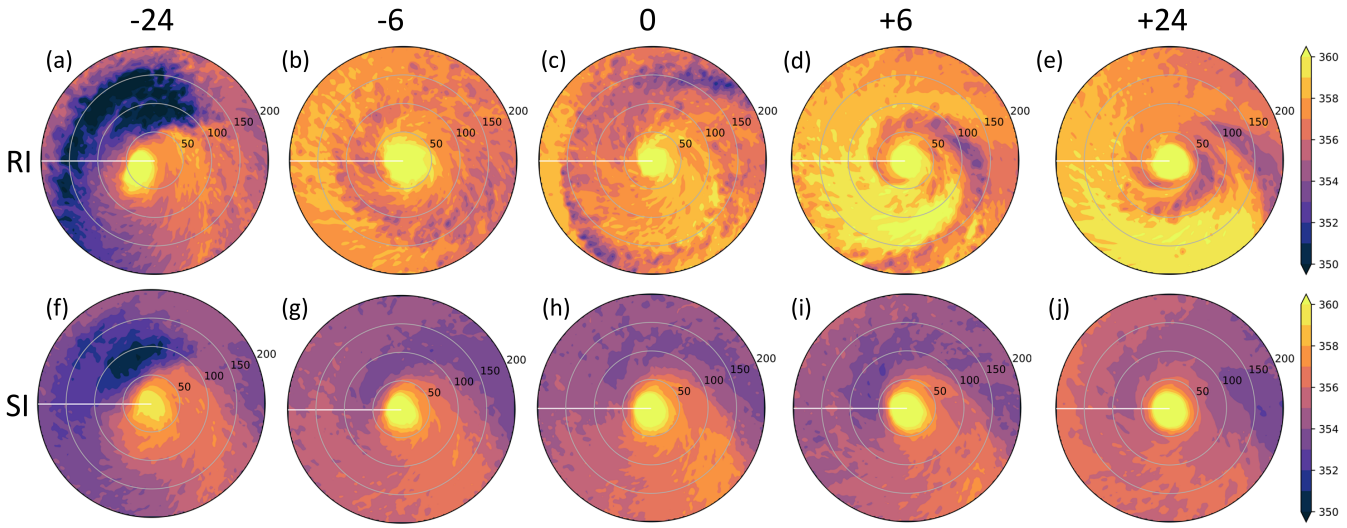


FIGURE 15 Surface equivalent potential temperature (θ_e, K) for ensemble average and times as in Figure 14. [Colour figure can be viewed at wileyonlinelibrary.com]

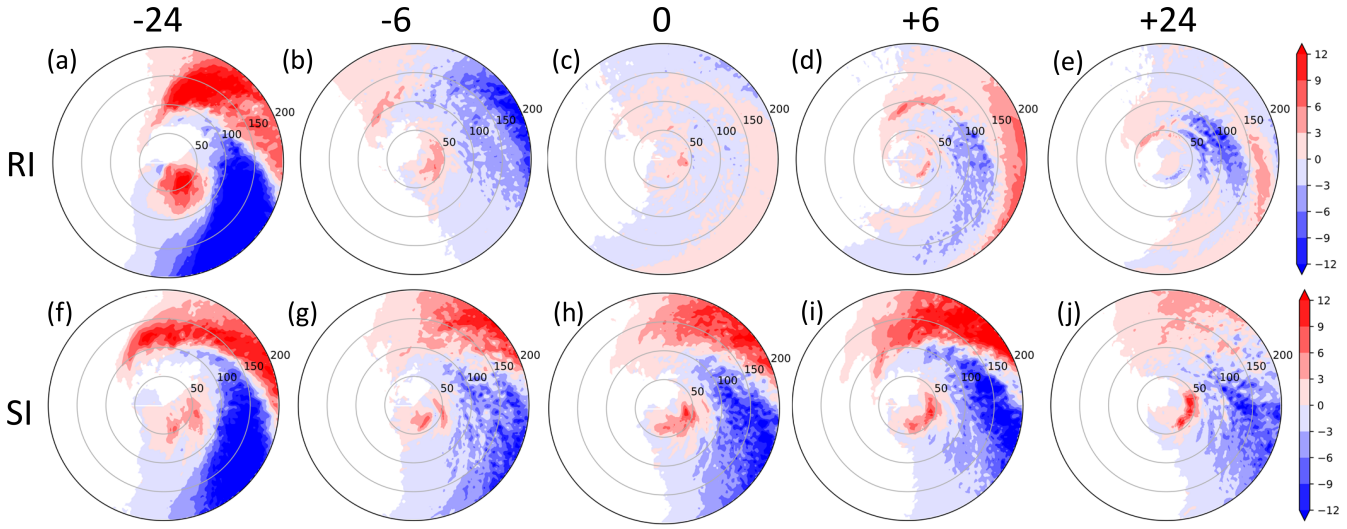


FIGURE 16 Ensemble averaged radial ventilation (kg·K·m^{-2} s^{-1}) averaged between heights of 1 and 3 km for times as in Figure 14. [Colour figure can be viewed at wileyonlinelibrary.com]

+24 hours (Figure 16g–j). Throughout RI, the magnitude of ventilation remains considerably lower than that of the SI ensemble (Figure 16c–e).

Upper-level radial ventilation is maximized upshear with the SI ensemble having a larger magnitude (Figure 17). In the day leading to onset, ventilation decreases substantially in the RI ensemble and most of the area is covered by the lightest shading through intensification (Figure 17a–e). However, it only marginally decreases in the SI ensemble and peaks within 50 km of the upshear right region (Figure 17g–i).

Overall, the ventilation analysis shows that the SI ensemble has greater downdraft and radial ventilation than the RI ensemble. The lower-level ventilation left of shear and the upper-level ventilation right of shear is consistent with previous studies (Alland *et al.*, 2021b). RI has been found to occur when there is mid-tropospheric moistening in the upshear quadrants (e.g., Nebylitsa *et al.*, 2023). Therefore, the persistence of the upper-level radial ventilation in the upshear right quadrant within the inner 50 km may explain why the SI ensemble exhibited lower intensification rates.

6 | CONCLUDING REMARKS

Climatologically averaged wind, moisture, and temperature profiles of different intensifying storms from reanalysis have been used to produce two ensembles of idealized TCs with different maximum intensification rates. This

1477870x, 0, Downloaded from https://rmets.onlinelibrary.wiley.com/doi/10.1002/qj.5011 by University Of Miami - Law, Wiley Online Library on [22/08/2025]. See the Terms and Conditions (https://onlinelibrary.wiley.com/terms-and-conditions) on Wiley Online Library for rules of use; OA articles are governed by the applicable Creative Commons License

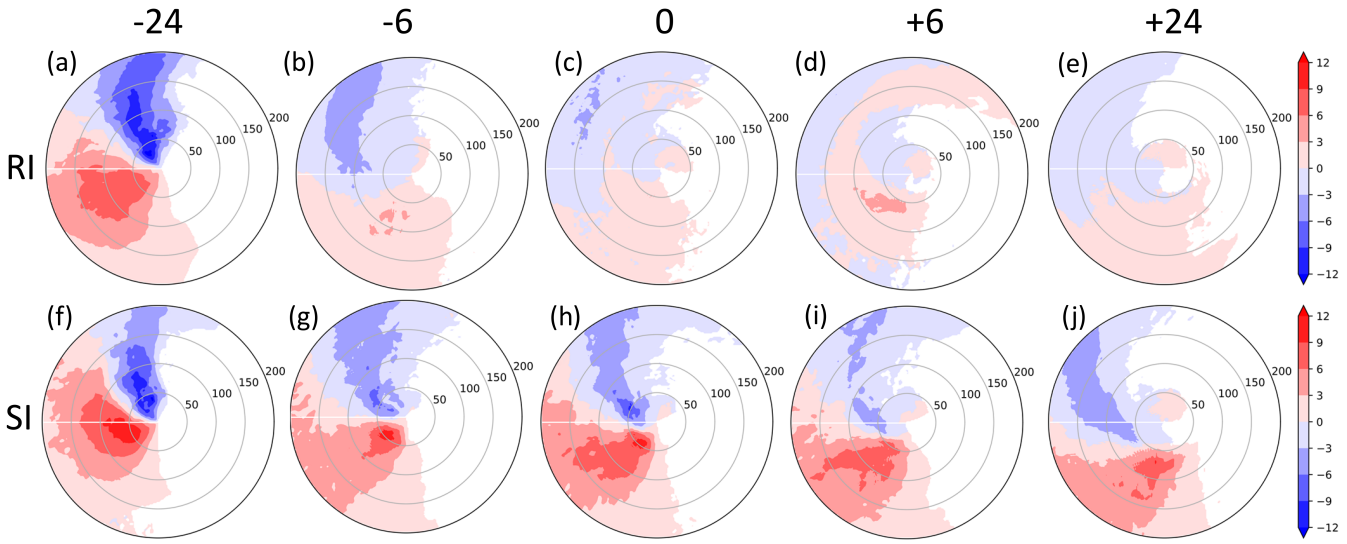


FIGURE 17 Ensemble averaged radial ventilation (kg·K·m^{-2} s^{-1}) averaged between heights of 5 and 9 km for times as in Figure 14. [Colour figure can be viewed at wileyonlinelibrary.com]

study showed that using TC-relative environments in idealized modeling can provide insight into the different mechanisms of intensification that may not have been possible using simplified environmental profiles. Previous studies have typically grouped storms as intensifying (usually through RI) or non-intensifying, steady-state storms. We have effectively produced two different sets of intensifying storms, one undergoing RI and one undergoing a smaller maximum intensification rate with an average difference of about 20 kts·24 hr^{-1}. The evolution of the storm structure through tilt and asymmetries, along with the influence of ventilation on intensification, was evaluated.

The onset of RI was characterized by a lower tilt, lower asymmetry, and less dry air ventilation as compared to the onset of SI and corroborates the results of previous modeling studies (e.g., Alland *et al.*, 2021a, b; Alvey III *et al.*, 2020; Finocchio & Rios-Berrios, 2021; Richardson *et al.*, 2022). The tilt and asymmetry around onset and through the intensification process was found to be statistically significantly different between the two ensembles. Both ensembles were very similar in tilt and asymmetry only a day prior to onset, with the RI ensemble exhibiting larger tilt and asymmetries between 12 and 24 hours pre onset. The rapid decrease in tilt and symmeterization of reflectivity of the RI ensemble in the 12 hours pre onset provides a small, yet vital window for accurate forecasting of future intensification rates. Differences in the ensembles during the first half of the intensification period may also provide beneficial information on how fast the TC may intensify. Despite both ensembles having low (<20 km) tilt throughout intensification, the SI ensemble experiences more variability in the tilt than the RI ensemble. This temporal variability, as well as larger ensemble spread of the vertical alignment, might induce a less effective transfer of energy into the TC, as tilt variations may allow for more ventilation (Finocchio *et al.*, 2016), resulting in a lower intensification rate, as compared to the RI ensemble which showcases a steady vertical alignment. A more thorough investigation is needed into connecting the rate of tilt and asymmetry change with intensification rate, particularly through observations through the TC-RADAR dataset (Fischer *et al.*, 2022).

The developed asymmetry parameter based on the near-surface reflectivity around the inner core of the storm was able to detect the nuances in the inner-core structure, even though all ensemble members had a visually apparent eye and azimuthal coverage of precipitation 12 hours into intensification. SI members exhibited less azimuthal and radial coverage of precipitation, especially right of shear, leading to higher asymmetry. The moistening of the upshear region has been found to precede intensification events (e.g., Nebylitsa *et al.*, 2023; Rios-Berrios *et al.*, 2016b), and the inability of the SI ensemble members to completely fill the upshear right region is a harbinger of a lower intensification rate. The lack of upshear moistening in the SI ensemble was also evident in the radial ventilation analysis. Upper-level radial ventilation peaked within 50 km of the center in the upshear right region whereas lower-level radial ventilation was persistent right of shear near the TC center. Downdraft ventilation is more abundant left of shear in the SI ensemble for all times.

CFADs of vertical velocity indicated that RI cases have more updrafts and SI cases have more downdrafts pre onset, but following intensification, there is an increase in upper-level vertical motion for the SI storms. This may allow for the increased upper-level reflectivity values in the

1477870x, 0, Downloaded from https://rmets.onlinelibrary.wiley.com/doi/10.1002/qj.5011 by University Of Miami - Law, Wiley Online Library on [22/08/2025]. See the Terms and Conditions (https://onlinelibrary.wiley.com/terms-and-conditions) on Wiley Online Library for rules of use; OA articles are governed by the applicable Creative Commons License

SI cases post onset compared to RI. Overall, the CFADs of reflectivity signified that RI TCs have a greater number of points with higher reflectivities compared to SI TCs. A more in-depth analysis of the microphysical differences between the RI and SI cases will be done in a future study.

The focus of this study was to discriminate between RI and SI events based solely on the prescribed difference between their environmental wind, temperature, and moisture profiles. We recognize that environmental conditions alone cannot cleanly differentiate intensification rates, and including other factors, for example vortex asymmetries at initialization, can lead to a deeper understanding of the differences between intensification rates. We also acknowledge that the SI ensemble in this study still intensifies at a moderate rate and more testing is needed to accurately assess slowly intensifying storms. The difficulty in achieving a non-RI hurricane is related to the rarity of the event and the specific conditions necessary. Furthermore, the results are dependent on the onset definition used in this study and thus the exact timing of the rapid alignment and symmeterization may vary slightly if another definition was used. This reveals the difficulty in predicting RI versus SI events, as 24 hours prior to onset, all ensemble members exhibit similar structural and thermodynamic properties. Nonetheless, we have demonstrated that there are differences in the few hours leading up to and during the intensification process that allow some storms to undergo more RI than others. This study also provides a pathway to investigating TCs in an idealized framework with more realistic environments as compared to previous studies.

ACKNOWLEDGEMENTS

The authors acknowledge four anonymous reviewers whose comments helped improve the manuscript. The authors acknowledge support from the Office of Naval Research grant N00014-20-1-2075, via the Tropical Cyclone Rapid Intensification (TCRI) Departmental Research Initiative. The authors acknowledge Dr Yi Dai who provided the code for the cold wake adjustment. The WRF simulations used in this study were produced at the Institute for Data Science and Computing (IDSC) at the University of Miami.

FUNDING INFORMATION

The authors acknowledge support from the Office of Naval Research grant N00014-20-1-2075, via the Tropical Cyclone Rapid Intensification (TCRI) Departmental Research Initiative.

DATA AVAILABILITY STATEMENT

The simulations used in this study are archived at the Institute for Data Science and Computing at the University of Miami and can be obtained through online transfer by coordination with the first author. Data analysis code is available in the same location. Tropical cyclone best-track data are available from the National Hurricane Center best track database at https://www.nhc.noaa.gov/data/. ERA5 data are available through the Climate Data Store at https://cds.climate.copernicus.eu/.

ORCID

Samantha Nebylitsa https://orcid.org/0000-0003-0639-1703
David S. Nolan https://orcid.org/0000-0003-0183-056X
Sharanya J. Majumdar https://orcid.org/0000-0001-8909-0927

REFERENCES

Alland, J.J., Tang, B.H., Corbosiero, K.L. & Bryan, G.H. (2021a) Combined effects of midlevel dry air and vertical wind shear on tropical cyclone development. Part I: downdraft ventilation. *Journal of the Atmospheric Sciences*, 78, 763–782. Available from: https://doi.org/10.1175/JAS-D-20-0054.1

Alland, J.J., Tang, B.H., Corbosiero, K.L. & Bryan, G.H. (2021b) Combined effects of midlevel dry air and vertical wind shear on tropical cyclone development. Part II: radial ventilation. *Journal of the Atmospheric Sciences*, 78, 783–796. Available from: https://doi.org/10.1175/JAS-D-20-0055.1

Alvey, G.R., III, Zawislak, J. & Zipser, E. (2015) Precipitation properties observed during tropical cyclone intensity change. *Monthly Weather Review*, 143(11), 4476–4492. Available from: https://doi.org/10.1175/MWR-D-15-0065.1

Alvey, G.R., III, Zipser, E. & Zawislak, J. (2020) How does hurricane Edouard (2014) evolve toward symmetry before rapid intensification? A high-resolution ensemble study. *Journal of the Atmospheric Sciences*, 77(4), 1329–1351. Available from: https://doi.org/10.1175/JAS-D-18-0355.1

Chen, S., Campbell, T.J., Jin, H., Gaberšek, S., Hodur, R.M. & Martin, P. (2010) Effect of two-way air–sea coupling in high and low wind speed regimes. *Monthly Weather Review*, 138(9), 3579–3602. Available from: https://doi.org/10.1175/2009MWR3119.1

Chen, S.S., Knaff, J.A. & Marks, F.D. (2006) Effects of vertical wind shear and storm motion on tropical cyclone rainfall asymmetries deduced from TRMM. *Monthly Weather Review*, 134(11), 3190–3208. Available from: https://doi.org/10.1175/MWR3245.1

Chen, X., Rozoff, C.M., Rogers, R.F., Corbosiero, K.L., Tao, D., Gu, J.F. et al. (2023) Research advances on internal processes affecting tropical cyclone intensity change from 2018–2022. *Tropical Cyclone Research and Review*, 12(1), 10–29. Available from: https://doi.org/10.1016/j.tcrr.2023.05.001

Corbosiero, K.L. & Molinari, J. (2002) The effects of vertical wind shear on the distribution of convection in tropical cyclones. *Monthly Weather Review*, 130(8), 2110–2123. Available from: https://doi.org/10.1175/1520-0493(2002)130<2110:TEOVWS>2.0.CO;2

Cram, T.A., Persing, J., Montgomery, M.T. & Braun, S.A. (2007) A Lagrangian trajectory view on transport and mixing processes between the eye, eyewall, and environment using a

1477870x, 0, Downloaded from https://rmets.onlinelibrary.wiley.com/doi/10.1002/qj.5011 by University Of Miami - Law, Wiley Online Library on [22/08/2025]. See the Terms and Conditions (https://onlinelibrary.wiley.com/terms-and-conditions) on Wiley Online Library for rules of use; OA articles are governed by the applicable Creative Commons License

high-resolution simulation of hurricane Bonnie (1998). *Journal of the Atmospheric Sciences*, 64(6), 1835–1856. Available from: https://doi.org/10.1175/JAS3921.1

Dai, Y., Torn, M.S., Williams, I.N. & Collins, W.D. (2023) Longwave radiative effects beyond the initial intensification phase of tropical cyclones. *Journal of the Atmospheric Sciences*, 80(7), 1829–1845. Available from: https://doi.org/10.1175/JAS-D-22-0214.1

DeHart, J.C., Houze, R.A. & Rogers, R.F. (2014) Quadrant distribution of tropical cyclone inner-core kinematics in relation to environmental shear. *Journal of the Atmospheric Sciences*, 71(7), 2713–2732. Available from: https://doi.org/10.1175/JAS-D-13-0298.1

DeMaria, M. (1996) The effect of vertical shear on tropical cyclone intensity change. *Journal of Atmospheric Sciences*, 53(14), 2076–2088. Available from: https://doi.org/10.1175/1520-0469(1996)053<2076:TEOVSO>2.0.CO;2

DeMaria, M. (2010) 9C. 5 Tropical cyclone intensity change predictability estimates using a statistical-dynamical model. In AMS 29th Conference on Hurricanes and Tropical Meteorology, May 10-14, 2010, Tucson, AZ.

DeMaria, M. & Kaplan, J. (1994) A statistical hurricane intensity prediction scheme (SHIPS) for the Atlantic basin. *Weather and Forecasting*, 9(2), 209–220. Available from: https://doi.org/10.1175/1520-0434(1994)009<0209:ASHIPS>2.0.CO;2

Dunion, J.P. (2011) Rewriting the climatology of the tropical North Atlantic and Caribbean Sea atmosphere. *Journal of Climate*, 24(3), 893–908. Available from: https://doi.org/10.1175/2010JCLI3496.1

Emanuel, K.A. (1986) An air-sea interaction theory for tropical cyclones. Part I: steady-state maintenance. *Journal of Atmospheric Sciences*, 43(6), 585–605. Available from: https://doi.org/10.1175/1520-0469(1986)043<0585:AASITF>2.0.CO;2

Finocchio, P.M. & Majumdar, S.J. (2017) The predictability of idealized tropical cyclones in environments with time-varying vertical wind shear. *Journal of Advances in Modeling Earth Systems*, 9(8), 2836–2862. Available from: https://doi.org/10.1002/2017MS001168

Finocchio, P.M., Majumdar, S.J., Nolan, D.S. & Iskandarani, M. (2016) Idealized tropical cyclone responses to the height and depth of environmental vertical wind shear. *Monthly Weather Review*, 144(6), 2155–2175. Available from: https://doi.org/10.1175/MWR-D-15-0320.1

Finocchio, P.M. & Rios-Berrios, R. (2021) The intensity-and size-dependent response of tropical cyclones to increasing vertical wind shear. *Journal of the Atmospheric Sciences*, 78(11), 3673–3690. Available from: https://doi.org/10.1175/JAS-D-21-0126.1

Fischer, M.S., Reasor, P.D., Rogers, R.F. & Gamache, J.F. (2022) An analysis of tropical cyclone vortex and convective characteristics in relation to storm intensity using a novel airborne Doppler radar database. *Monthly Weather Review*, 150(9), 2255–2278. Available from: https://doi.org/10.1175/MWR-D-21-0223.1

Fischer, M.S., Reasor, P.D., Tang, B.H., Corbosiero, K.L., Torn, R.D. & Chen, X. (2023) A tale of two vortex evolutions: using a high-resolution ensemble to assess the impacts of ventilation on a tropical cyclone rapid intensification event. *Monthly Weather Review*, 151(1), 297–320. Available from: https://doi.org/10.1175/MWR-D-22-0037.1

Fischer, M.S., Rogers, R.F., Reasor, P.D. & Dunion, J.P. (2024) An observational analysis of the relationship between tropical cyclone vortex tilt, precipitation structure, and intensity change. *Monthly Weather Review*, 152(1), 203–225. Available from: https://doi.org/10.1175/MWR-D-23-0089.1

Frank, W.M. & Ritchie, E.A. (1999) Effects of environmental flow upon tropical cyclone structure. *Monthly Weather Review*, 127(9), 2044–2061. Available from: https://doi.org/10.1175/1520-0493(1999)127<2044:EOEFUT>2.0.CO;2

Frank, W.M. & Ritchie, E.A. (2001) Effects of vertical wind shear on the intensity and structure of numerically simulated hurricanes. *Monthly Weather Review*, 129(9), 2249–2269. Available from: https://doi.org/10.1175/1520-0493(2001)129<2249:EOVWSO>2.0.CO;2

Hendricks, E.A., Peng, M.S., Fu, B. & Li, T. (2010) Quantifying environmental control on tropical cyclone intensity change. *Monthly Weather Review*, 138(8), 3243–3271. Available from: https://doi.org/10.1175/2010MWR3185.1

Hersbach, H., Bell, B., Berrisford, P., Hirahara, S., Horanyi, A., Munoz-Sabater, J. et al. (2020) The ERA5 global reanalysis. *Quarterly Journal of the Royal Meteorological Society*, 146(730), 1999–2049. Available from: https://doi.org/10.1002/qj.3803

Hong, S.Y., Noh, Y. & Dudhia, J. (2006) A new vertical diffusion package with an explicit treatment of entrainment processes. *Monthly Weather Review*, 134, 2318–2341.

Iacono, M.J., Delamere, J.S., Mlawer, E.J., Shephard, M.W., Clough, S.A. & Collins, W.D. (2008) Radiative forcing by long-lived greenhouse gases: calculations with the AER radiative transfer models. *Journal of Geophysical Research: Atmospheres*, 113(D13). Available from: https://doi.org/10.1029/2008JD009944

Jones, S.C. (1995) The evolution of vortices in vertical shear. I: initially barotropic vortices. *Quarterly Journal of the Royal Meteorological Society*, 121(524), 821–851. Available from: https://doi.org/10.1002/qj.49712152406

Judt, F., Rios-Berrios, R. & Bryan, G.H. (2023) Marathon versus sprint: two modes of tropical cyclone rapid intensification in a global convection-permitting simulation. *Monthly Weather Review*, 151(10), 2683–2699. Available from: https://doi.org/10.1175/MWR-D-23-0038.1

Kaplan, J. & DeMaria, M. (2003) Large-scale characteristics of rapidly intensifying tropical cyclones in the North Atlantic basin. *Weather and Forecasting*, 18(6), 1093–1108. Available from: https://doi.org/10.1175/1520-0434(2003)018<1093:LCORIT>2.0.CO;2

Kaplan, J., DeMaria, M. & Knaff, J.A. (2010) A revised tropical cyclone rapid intensification index for the Atlantic and eastern North Pacific basins. *Weather and Forecasting*, 25(1), 220–241. Available from: https://doi.org/10.1175/2009WAF2222280.1

Kwon, Y.C. & Frank, W.M. (2008) Dynamic instabilities of simulated hurricane-like vortices and their impacts on the core structure of hurricanes. Part II: moist experiments. *Journal of the Atmospheric Sciences*, 65(1), 106–122. Available from: https://doi.org/10.1175/2007JAS2132.1

Landsea, C.W. & Franklin, J.L. (2013) Atlantic hurricane database uncertainty and presentation of a new database format. *Monthly Weather Review*, 141(10), 3576–3592. Available from: https://doi.org/10.1175/MWR-D-12-00254.1

Lee, C.Y., Tippett, M.K., Sobel, A.H. & Camargo, S.J. (2016) Rapid intensification and the bimodal distribution of tropical cyclone intensity. *Nature Communications*, 7(1), 10625.

1477870x, 0, Downloaded from https://rmets.onlinelibrary.wiley.com/doi/10.1002/qj.5011 by University Of Miami - Law, Wiley Online Library on [22/08/2025]. See the Terms and Conditions (https://onlinelibrary.wiley.com/terms-and-conditions) on Wiley Online Library for rules of use; OA articles are governed by the applicable Creative Commons License

Majumdar, S.J., Nebylitsa, S., Klozbach, P.J., Masiello, C. & Michael, Z.R. (2023) North Atlantic tropical cyclone intensification: regional drivers and trends. *Geophysical Review Letters*, 50(17), e2023GL104803. Available from: https://doi.org/10.1029/2023GL104803

Marín, J.C., Raymond, D.J. & Raga, G.B. (2009) Intensification of tropical cyclones in the GFS model. *Atmospheric Chemistry and Physics*, 9(4), 1407–1417. Available from: https://doi.org/10.5194/acp-9-1407-2009

Marks, F.D., Houze, R.A. & Gamache, J.F. (1992) Dual-aircraft investigation of the inner core of hurricane Norbert. Part I: kinematic structure. *Journal of the Atmospheric Sciences*, 49(11), 919–942. Available from: https://doi.org/10.1175/1520-0469(1992)049<0919:DAIOTI>2.0.CO;2

McGauley, M.G. & Nolan, D.S. (2011) Measuring environmental favorability for tropical cyclogenesis by statistical analysis of threshold parameters. *Journal of Climate*, 24(23), 5968–5997. Available from: https://doi.org/10.1175/2011JCLI4176.1

Miyamoto, Y. & Nolan, D.S. (2018) Structural changes preceding rapid intensification in tropical cyclones as shown in a large ensemble of idealized simulations. *Journal of the Atmospheric Sciences*, 75(2), 555–569. Available from: https://doi.org/10.1175/JAS-D-17-0177.1

Miyamoto, Y. & Takemi, T. (2013) A transition mechanism for the spontaneous axisymmetric intensification of tropical cyclones. *Journal of the Atmospheric Sciences*, 70(1), 112–129. Available from: https://doi.org/10.1175/JAS-D-11-0285.1

Molinari, J., Vollaro, D. & Corbosiero, K.L. (2004) Tropical cyclone formation in a sheared environment: a case study. *Journal of the Atmospheric Sciences*, 61(21), 2493–2509. Available from: https://doi.org/10.1175/JAS3291.1

Morrison, H., Curry, J.A. & Khvorostyanov, V.I. (2005) A new double-moment microphysics parameterization for application in cloud and climate models. Part I: description. *Journal of the Atmospheric Sciences*, 62, 1665–1677. Available from: https://doi.org/10.1175/JAS3446.1

Morrison, H., Thompson, G. & Tatarskii, V. (2009) Impact of cloud microphysics on the development of trailing stratiform precipitation in a simulated squall line: comparison of one-and two-moment schemes. *Monthly Weather Review*, 137(3), 991–1007.

Munsell, E.B., Zhang, F. & Stern, D.P. (2013) Predictability and dynamics of a nonintensifying tropical storm: Erika (2009). *Journal of the Atmospheric Sciences*, 70(8), 2505–2524. Available from: https://doi.org/10.1175/JAS-D-12-0243.1

Nebylitsa, S., Majumdar, S.J. & Nolan, D.S. (2023) Revisiting environmental wind and moisture calculations in the context of tropical cyclone intensification. *Weather and Forecasting*, 38(10), 2077–2094. Available from: https://doi.org/10.1175/WAF-D-23-0045.1

Nguyen, L.T., Molinari, J. & Thomas, D. (2014) Evaluation of tropical cyclone center identification methods in numerical models. *Monthly Weather Review*, 142(11), 4326–4339. Available from: https://doi.org/10.1175/MWR-D-14-00044.1

Nolan, D.S., Atlas, R., Bhatia, K.T. & Bucci, L.R. (2013) Development and validation of a hurricane nature run using the joint OSSE nature run and the WRF model. *Journal of Advances in Modeling Earth Systems*, 5, 382–405. Available from: https://doi.org/10.1002/jame.20031

Nolan, D.S., Nebylitsa, S., McNoldy, B.D. & Majumdar, S.J. (2024) Modulation of tropical cyclone rapid intensification by mesoscale asymmetries. *Quarterly Journal of the Royal Meteorological Society*, 150(758), 388–415. Available from: https://doi.org/10.1002/qj.4602

Onderlinde, M.J. & Nolan, D.S. (2016) Tropical cyclone–relative environmental helicity and the pathways to intensification in shear. *Journal of the Atmospheric Sciences*, 73(2), 869–890. Available from: https://doi.org/10.1175/JAS-D-15-0261.1

Onderlinde, M.J. & Nolan, D.S. (2017) The tropical cyclone response to changing wind shear using the method of time-varying point-downscaling. *Journal of Advances in Modeling Earth Systems*, 9(2), 908–931. Available from: https://doi.org/10.1002/2016MS000796

Rappin, E.D. & Nolan, D.S. (2012) The effect of vertical shear orientation on tropical cyclogenesis. *Quarterly Journal of the Royal Meteorological Society*, 138(665), 1035–1054. Available from: https://doi.org/10.1002/qj.977

Richardson, J.C., Torn, R.D. & Tang, B.H. (2022) An analog comparison between rapidly and slowly intensifying tropical cyclones. *Monthly Weather Review*, 150(8), 2139–2156. Available from: https://doi.org/10.1175/MWR-D-21-0260.1

Riemer, M., Montgomery, M.T. & Nicholls, M.E. (2010) A new paradigm for intensity modification of tropical cyclones: thermodynamic impact of vertical wind shear on the inflow layer. *Atmospheric Chemistry and Physics*, 10(7), 3163–3188. Available from: https://doi.org/10.5194/acp-10-3163-2010

Rios-Berrios, R. (2020) Impacts of radiation and cold pools on the intensity and vortex tilt of weak tropical cyclones interacting with vertical wind shear. *Journal of the Atmospheric Sciences*, 77(2), 669–689. Available from: https://doi.org/10.1175/JAS-D-19-0159.1

Rios-Berrios, R., Davis, C.A. & Torn, R.D. (2018) A hypothesis for the intensification of tropical cyclones under moderate vertical wind shear. *Journal of the Atmospheric Sciences*, 75(12), 4149–4173. Available from: https://doi.org/10.1175/JAS-D-18-0070.1

Rios-Berrios, R., Finocchio, P.M., Alland, J.J., Chen, X., Fischer, M.S., Stevenson, S.N. et al. (2024) A review of the interactions between tropical cyclones and environmental vertical wind shear. *Journal of the Atmospheric Sciences*, 81(4), 713–741. Available from: https://doi.org/10.1175/JAS-D-23-0022.1

Rios-Berrios, R. & Torn, R.D. (2017) Climatological analysis of tropical cyclone intensity changes under moderate vertical wind shear. *Monthly Weather Review*, 145(5), 1717–1738. Available from: https://doi.org/10.1175/MWR-D-16-0350.1

Rios-Berrios, R., Torn, R.D. & Davis, C.A. (2016a) An ensemble approach to investigate tropical cyclone intensification in sheared environments. Part I: Katia (2011). *Journal of the Atmospheric Sciences*, 73(1), 71–93. Available from: https://doi.org/10.1175/JAS-D-15-0052.1

Rios-Berrios, R., Torn, R.D. & Davis, C.A. (2016b) An ensemble approach to investigate tropical cyclone intensification in sheared environments. Part II: Ophelia (2011). *Journal of the Atmospheric Sciences*, 73(4), 1555–1575. Available from: https://doi.org/10.1175/JAS-D-15-0245.1

Rogers, R., Reasor, P. & Lorsolo, S. (2013) Airborne Doppler observations of the inner-core structural differences between intensifying and steady-state tropical cyclones. *Monthly Weather Review*, 141(9), 2970–2991. Available from: https://doi.org/10.1175/MWR-D-12-00357.1

1477870x, 0, Downloaded from https://rmets.onlinelibrary.wiley.com/doi/10.1002/qj.5011 by University Of Miami - Law, Wiley Online Library on [22/08/2025]. See the Terms and Conditions (https://onlinelibrary.wiley.com/terms-and-conditions) on Wiley Online Library for rules of use; OA articles are governed by the applicable Creative Commons License

Ruppert, J.H., Jr., Wing, A.A., Tang, X. & Duran, E.L. (2020) The critical role of cloud–infrared radiation feedback in tropical cyclone development. *Proceedings of the National Academy of Sciences*, 117(45), 27884–27892. Available from: https://doi.org/10.1073/pnas.2013584117

Schecter, D.A. (2022) Intensification of tilted tropical cyclones over relatively cool and warm oceans in idealized numerical simulations. *Journal of the Atmospheric Sciences*, 79(2), 485–512. Available from: https://doi.org/10.1175/JAS-D-21-0051.1

Simpson, R.H., Bureau, U.W. & Riehl, H. (1958) Mid-tropospheric ventilation as a constraint on hurricane development and maintenance. Proc. Tech. Conf. on Hurricanes, Miami Beach, FL, Amer. Meteor. Soc., D4-1-D4-10.

Skamarock, W.C., Klemp, J.B., Dudhia, J., Gill, D.O., Liu, Z., Berner, J. et al. (2019) A description of the advanced research WRF version 4. NCAR tech. note ncar/tn-556+ str, 145.

Stevenson, S.N., Corbosiero, K.L. & Abarca, S.F. (2016) Lightning in eastern North Pacific tropical cyclones: a comparison to the North Atlantic. *Monthly Weather Review*, 144(1), 225–239. Available from: https://doi.org/10.1175/MWR-D-15-0276.1

Tang, B. & Emanuel, K. (2010) Midlevel ventilation's constraint on tropical cyclone intensity. *Journal of the Atmospheric Sciences*, 67(6), 1817–1830. Available from: https://doi.org/10.1175/2010JAS3318.1

Tang, B. & Emanuel, K. (2012a) Sensitivity of tropical cyclone intensity to ventilation in an axisymmetric model. *Journal of the Atmospheric Sciences*, 69, 2394–2413. Available from: https://doi.org/10.1175/JAS-D-11-0232.1

Tang, B. & Emanuel, K. (2012b) A ventilation index for tropical cyclones. *Bulletin of the American Meteorological Society*, 93(12), 1901–1912. Available from: https://doi.org/10.1175/BAMS-D-11-00165.1

Tang, B.H., Rios-Berrios, R. & Zhang, J.A. (2024) Diagnosing radial ventilation in Dropsonde observations of hurricane Sam (2021). *Monthly Weather Review*, 152, 1725–1739. Available from: https://doi.org/10.1175/MWR-D-23-0224.1

Tao, D. & Zhang, F. (2014) Effect of environmental shear, sea-surface temperature, and ambient moisture on the formation and predictability of tropical cyclones: an ensemble-mean perspective. *Journal of Advances in Modeling Earth Systems*, 6(2), 384–404. Available from: https://doi.org/10.1002/2014MS000314

Tao, D. & Zhang, F. (2015) Effects of vertical wind shear on the predictability of tropical cyclones: practical versus intrinsic limit. *Journal of Advances in Modeling Earth Systems*, 7(4), 1534–1553. Available from: https://doi.org/10.1002/2015MS000474

Tiedtke, M. (1989) A comprehensive mass flux scheme for cumulus parameterization in large scale models. *Monthly Weather Review*, 117, 1779–1800.

Vigh, J.L. & Schubert, W.H. (2009) Rapid development of the tropical cyclone warm core. *Journal of the Atmospheric Sciences*, 66(11), 3335–3350. Available from: https://doi.org/10.1175/2009JAS3092.1

Wadler, J.B., Rudzin, J.E., de la Cruz, B.J., Chen, J., Fischer, M., Chen, G. et al. (2023) A review of recent research progress on the effect of external influences on tropical cyclone intensity change. *Tropical Cyclone Research and Review*, 12(3), 200–215. Available from: https://doi.org/10.1016/j.tcrr.2023.09.001

Wang, Y., Zhou, L. & Hamilton, K. (2007) Effect of convective entrainment/detrainment on the simulation of the tropical precipitation diurnal cycle. *Monthly Weather Review*, 135, 567–585.

Yu, C.L., Tang, B. & Fovell, R.G. (2023) Diverging behaviors of simulated tropical cyclones in moderate vertical wind shear. *Journal of the Atmospheric Sciences*, 80(12), 2837–2860. Available from: https://doi.org/10.1175/JAS-D-23-0048.1

Yuter, S.E. & Houze, R.A., Jr. (1995) Three-dimensional kinematic and microphysical evolution of Florida cumulonimbus. Part II: frequency distributions of vertical velocity, reflectivity, and differential reflectivity. *Monthly Weather Review*, 123(7), 1941–1963. Available from: https://doi.org/10.1175/1520-0493(1995)123<1941:TDKAME>2.0.CO;2

Zarzycki, C.M. (2016) Tropical cyclone intensity errors associated with lack of two-way ocean coupling in high-resolution global simulations. *Journal of Climate*, 29(23), 8589–8610. Available from: https://doi.org/10.1175/JCLI-D-16-0273.1

Zawislak, J., Jiang, H., Alvey, G.R., Zipser, E.J., Rogers, R.F., Zhang, J.A. et al. (2016) Observations of the structure and evolution of hurricane Edouard (2014) during intensity change. Part I: relationship between the thermodynamic structure and precipitation. *Monthly Weather Review*, 144(9), 3333–3354. Available from: https://doi.org/10.1175/MWR-D-16-0018.1

Zhang, F. & Tao, D. (2013) Effects of vertical wind shear on the predictability of tropical cyclones. *Journal of the Atmospheric Sciences*, 70(3), 975–983. Available from: https://doi.org/10.1175/JAS-D-12-0133.1

SUPPORTING INFORMATION

Additional supporting information can be found online in the Supporting Information section at the end of this article.

How to cite this article: Nebylitsa, S., Nolan, D.S., McNoldy, B.D. & Majumdar, S.J. (2025) Rapid versus slow intensification of idealized tropical cyclones using soundings from reanalysis. *Quarterly Journal of the Royal Meteorological Society*, e5011. Available from: https://doi.org/10.1002/qj.5011

1477870x, 0, Downloaded from https://rmets.onlinelibrary.wiley.com/doi/10.1002/qj.5011 by University Of Miami - Law, Wiley Online Library on [22/08/2025]. See the Terms and Conditions (https://onlinelibrary.wiley.com/terms-and-conditions) on Wiley Online Library for rules of use; OA articles are governed by the applicable Creative Commons License

APPENDIX A. ENVIRONMENTAL PROFILES

TABLE A1 The table below contains the climatological average in the 200–800-km radius for temperature, mixing ratio, and adjusted wind profiles used to create the rapidly (RI) and slowly (SI) intensifying environments that the model was continuously nudged onto.

		RI				SI			
Pressure (hPa)	Geopotential height (m)	Zonal wind ($m \cdot s^{-1}$)	Meridional wind ($m \cdot s^{-1}$)	Temperature (K)	Mixing ratio ($g \cdot kg^{-1}$)	Zonal wind ($m \cdot s^{-1}$)	Meridional wind ($m \cdot s^{-1}$)	Temperature (K)	Mixing ratio ($g \cdot kg^{-1}$)
100	16,571	−5.3682	−0.6284	196.86	0.004	−3.4466	−0.3299	198.84	0.004
125	15,276	−2.1947	−0.4661	198.98	0.005	0.4393	0.4862	200.62	0.005
150	14,196	−0.6607	0.8623	205.39	0.012	2.3475	1.8816	206.11	0.011
175	13,253	−0.4818	1.944	212.64	0.028	2.756	2.8308	212.69	0.025
200	12,409	−0.788	2.3606	219.64	0.06	2.44537	3.233	219.25	0.052
225	11,641	−1.1618	2.3076	226.07	0.112	1.8526	3.2342	225.43	0.097
250	10,937	−1.5336	1.9977	231.87	0.183	1.2668	3.0097	231.13	0.16
300	9675	−2.3286	1.4237	241.83	0.387	−0.2229	2.4292	241.06	0.344
350	8567	−3.0678	1.1751	250.06	0.696	−0.6824	2.0317	249.31	0.627
400	7577	−3.6318	1.1745	256.91	1.13	−1.49	1.8141	256.19	1.017
450	6883	−4.1698	1.2711	262.59	1.734	−2.2606	1.7363	261.93	1.541
500	5865	−4.636	1.4193	267.32	2.556	−2.9273	1.7968	266.74	2.264
550	5114	−4.9553	1.5891	271.4	3.562	−3.4651	1.9156	270.87	3.158
600	4418	−5.1635	1.7392	274.9	4.462	−3.8851	2.0303	274.46	4.015
650	3768	−5.4036	1.8804	278.66	5.362	−4.28	2.1245	278.16	4.884
700	3158	−5.7178	1.9627	282.29	6.522	−4.702	2.168	281.76	5.989
750	2583	−6.0425	1.9654	285.45	7.923	−5.1354	2.1391	285.94	7.332
775	2307	−6.1941	1.9423	286.89	8.682	−5.3461	2.0996	286.39	8.076
800	2039	−6.3499	1.9158	288.26	9.464	−5.5596	2.0516	287.76	8.853
825	1777	−6.5247	1.8878	289.57	10.279	−5.7786	1.9974	289.06	9.669
850	1523	−6.7238	1.8506	290.82	11.143	−6.0269	1.9352	290.3	10.536
925	795	−7.4099	1.5113	294.35	14.265	−6.8272	1.5589	293.72	13.637
1000	113	−7.3636	0.9381	298.89	16.889	−6.9732	0.9766	298.23	16.304

1477870x, 0, Downloaded from https://rmets.onlinelibrary.wiley.com/doi/10.1002/qj.5011 by University Of Miami - Law, Wiley Online Library on [22/08/2025]. See the Terms and Conditions (https://onlinelibrary.wiley.com/terms-and-conditions) on Wiley Online Library for rules of use; OA articles are governed by the applicable Creative Commons License